Partitioning riverine sulfate sources using oxygen and sulfur isotopes: Implications for carbon budgets of large rivers

K. E. Relph[a,*], E. I. Stevenson[a], A. V. Turchyn[a], G. Antler[b], M. J. Bickle[a], J. J. Baronas[a], S. E. Darby[c], D. R. Parsons[d], E. T. Tipper[a]

[a]*Department of Earth Sciences, University of Cambridge, Cambridge, CB2 3EQ, UK*
[b]*Department of Geological and Environmental Sciences, Ben-Gurion University of the Negev, Beersheba, Israel*
[c]*School of Geography and Environmental Science, University of Southampton, Southampton, SO17 1BJ, UK*
[d]*Energy and Environment Institute, University of Hull, Hull HU6 7RX, UK*

Abstract

The weathering of carbonate rocks with sulfuric acid releases carbon dioxide (CO_2) to the atmosphere, offsetting the CO_2 drawdown from carbonic acid weathering of silicates thought to regulate global climate. Quantifying CO_2 release from sulfuric acid weathering requires the partitioning of riverine sulfate between its two main sources: sedimentary sulfate and sulfide. Although the sulfur ($\delta^{34}S_{SO_4}$) and oxygen ($\delta^{18}O_{SO_4}$) isotope ratios of sedimentary sulfates (gypsum and anhydrite) of different ages are well constrained, the $\delta^{34}S$ of sulfide minerals is highly variable, restricting the utility of $\delta^{34}S$ for partitioning sulfur sources. Here, we use oxygen isotope ratios in the river water ($\delta^{18}O_{H_2O}$) and sulfate molecules ($\delta^{18}O_{SO_4}$) to partition the fraction of sulfate and associated uncertainty delivered by the oxidative weathering of pyrite (f_{pyr}). The partitioning is illustrated using the Mekong River, one of the world's largest river basins, presenting new $\delta^{18}O_{SO_4}$, $\delta^{18}O_{H_2O}$ and $\delta^{34}S_{SO_4}$ data collected on 18 tributaries and 6 main stem sites over two field seasons at peak flux. The geological, geomorphological and climatic diversity of the Mekong River Basin make it an ideal field site to quantify the role of sulfuric acid weathering and its implications for the carbon cycle. There is a 12‰ range in both the difference between $\delta^{18}O_{SO_4}$ and $\delta^{18}O_{H_2O}$ ($\Delta^{18}O_{SO_4-H_2O}$) and $\delta^{34}S$ in the river waters of the basin. In the Mekong tributaries, sources of sulfate are highly variable with the fraction of sulfate derived from pyrite oxidation (f_{pyr}) ranging from 0.19 to 0.84. In the mainstem, f_{pyr} reflects the flux-weighted mean of these tributary inputs, with 56±7% (1σ) of the sulfate delivered to the ocean at the Mekong mouth being derived from the oxidative weathering of pyrite. As a result, we estimate that ~70% of CO_2 consumed through silicate weathering in the Mekong basin is offset by the release of CO_2 via the dissolution of carbonates by sulfuric acid.

Keywords: sulfuric acid, pyrite oxidation, Mekong, oxygen isotopes, CO_2 release, chemical weathering

1. Introduction

Chemical weathering by carbonic acid is a major negative feedback thought to regulate Earth's climate over geological time (Walker *et al.*, 1981). However, there remain a number of major uncertainties in both the quantification of chemical weathering fluxes, their impact on atmospheric carbon dioxide, CO_2(g), and thus their impact on global climate. One process that may have an important impact on the calculation of chemical weathering fluxes is the weathering of carbonate rocks with sulfuric acid (H_2SO_4), predominantly derived from the oxidation of sedimentary pyrite (FeS_2, e.g., Francois & Walker, 1992; Torres *et al.*, 2014). This releases geologically stored carbon into the atmosphere as CO_2(g) by the following reaction (e.g., Spence & Telmer, 2005; Calmels *et al.*, 2007):

$$H_2SO_4 + CaCO_3 \Rightarrow CO_2(g) + H_2O + Ca^{2+} + SO_4^{2-} \quad (1)$$

Recent work has revealed that in several of the world's largest river basins, weathering of carbonate minerals driven by pyrite oxidation may release more CO_2 than is consumed via silicate weathering with carbonic acid (e.g., Calmels *et al.*, 2007; Torres *et al.*, 2016). However, quantifying the oxidative weathering of pyrite has proved challenging. This is because in large mixed lithology basins, not all riverine dissolved sulfate (SO_4^{2-}) is from the oxidative weathering of pyrite, but rather is derived from multiple sources such as gypsum ($CaSO_4{\cdot}2H_2O$) and anhydrite ($CaSO_4$) dissolution, atmospheric, and anthropogenic inputs (Robinson & Bottrell, 1997; Canfield, 2004). The supply of SO_4^{2-} from gypsum and anhydrite does not form sulfuric acid driving further mineral dissolution and therefore does not influence the carbon cycle. In contrast, the oxidation of pyrite and dissolution of atmospheric sulfur dioxide deliver SO_4^{2-} to the critical zone through the dissociation of sulfuric acid, which releases geologically stored CO_2 when it reacts with carbonate minerals (Eqn. 1). Moreover, anthropogenic exacerbation of reaction 1 through the burning of sulfurous coal, causing acid rain has been widely recorded in North America, China, and northern Europe (Menz & Seip, 2004; Li *et al.*, 2008; Li & Ji, 2016). Quantifying sulfuric acid weathering at a global scale is therefore critical, both in the context of understanding the natural silicate weathering-climate feedback, and in predicting

*Corresponding author
Email address: katy@relphs.co.uk (K. E. Relph)

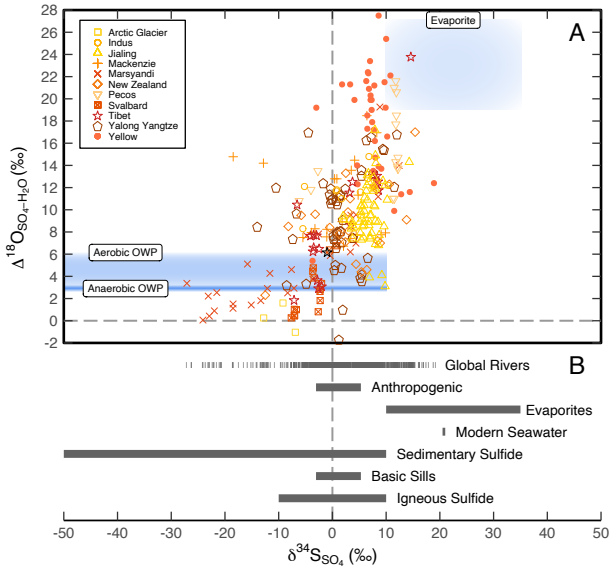

Figure 1: A) Global river waters form a mixing array in $\delta^{34}S$, $\Delta^{18}O_{SO_4-H_2O}$ ($\delta^{18}O_{SO_4}$ relative to local meteoric water $\delta^{18}O_{H_2O}$) space, between two distinct end members: evaporites and sedimentary sulfides (specifically the oxidative weathering of pyrite). Sedimentary sulfide $\Delta^{18}O_{SO_4-H_2O}$ illustrated for a range from 2.9‰ (for anaerobically oxidised pyrite) to 6.2‰ (for a maximum of 17% atmospheric O_2 at 23‰ incorporation during aerobic oxidative weathering of pyrite). Evaporite $\Delta^{18}O_{SO_4-H_2O}$ varies, depending on sedimentary deposit age, from 19‰ to 27‰ (Claypool *et al.*, 1980). End-members are relative to the average of the river water $\delta^{18}O_{H_2O}$ value of -9.1‰. B) Global rivers span a large range of $\delta^{34}S_{SO_4}$, however there is overlap between the many sources of sulfur (sources of data given in SI 1).

the impact of additional anthropogenically sourced sulfuric acid.

Several methods have been proposed to track the origin of riverine dissolved SO_4^{2-}, including the ratio of SO_4^{2-} to bicarbonate (HCO_3^-) coupled to stable carbon isotope ratios ($\delta^{13}C$, e.g., Spence & Telmer, 2005; Li *et al.*, 2008), inverse methods based on rock ratios (e.g., Torres *et al.*, 2016; Kemeny *et al.*, 2021) and sulfur isotope ratios ($\delta^{34}S_{SO_4}$) sometimes coupled with the oxygen isotope ratio of the SO_4^{2-} molecule ($\delta^{18}O_{SO_4}$, Calmels *et al.*, 2007; Turchyn *et al.*, 2013).

Sulfur isotope ratios of dissolved SO_4^{2-} ($\delta^{34}S_{SO_4}$) reflect the origin of the SO_4^{2-} since there is minimal S-isotope fractionation between the sulfur mineral source and SO_4^{2-} (Claypool *et al.*, 1980; Thode, 1991; Balci *et al.*, 2007; Heidel & Tichomirowa, 2011).Since sedimentary sulfide and sulfate minerals have broadly differing $\delta^{34}S$ compositions (Fig. 1), the use of $\delta^{34}S_{SO_4}$ to determine the source of riverine dissolved SO_4^{2-} is attractive because there is a large range of ca. 40‰ in $\delta^{34}S_{SO_4}$ in global rivers (Burke *et al.*, 2018). However, the global variation in $\delta^{34}S$ signatures of pyrite is even greater, meaning that unless the local composition of pyrite is well known (and is distinct from other local SO_4^{2-} sources, Fig. 1B) there is a large uncertainty in using $\delta^{34}S_{SO_4}$ to partition dissolved SO_4^{2-} between sources. The $\delta^{34}S$ of pyrite is difficult to constrain in most river catchments because pyrite is one of the most reactive mineral phases at Earth surface conditions (Brantley *et al.*, 2013) and is usually no longer present in river sediments that are commonly used to provide an average composition of the local catchment lithologies (Garzanti & Resentini, 2016). Whilst the significance of pyrite weathering has been demonstrated in small to medium catchments with restricted SO_4^{2-} sources (e.g.; Spence & Telmer, 2005; Galy & France-Lanord, 1999), an assessment of the significance of sulfuric acid weathering has only been made for a handful of the world's largest rivers (e.g., Calmels *et al.*, 2007; Torres *et al.*, 2016; Horan *et al.*, 2019).

Oxygen isotope ratios offer a powerful tool to constrain the origin of riverine SO_4^{2-} because $\delta^{18}O_{SO_4}$ is inherited from the $\delta^{18}O$ of the oxygen that was incorporated into the SO_4^{2-} ion at the time that the S-O bond was formed (Claypool *et al.*, 1980; van Everdingen & Krouse, 1985). Once formed, the S-O bond is largely fixed at surface temperatures. Thus, sulfide-derived SO_4^{2-} retains a $\delta^{18}O$ signature of meteoric water and molecular O_2 from the critical zone, while the oxygen in evaporite-derived SO_4^{2-} retains the signature of the seawater from the time of deposition (in addition to a small degree of isotopic fractionation, Claypool *et al.*, 1980; Strauss, 1997). Global rivers define a broad array between $\delta^{34}S$ and $\delta^{18}O_{SO_4}$, normalised to local meteoric water ($\Delta^{18}O_{SO_4-H_2O}$, Fig. 1A,), suggesting a mixing trend between sulfate derived from sedimentary sulfate and sulfide mineral sources.

In this contribution oxygen isotope ratios in water ($\delta^{18}O_{H_2O}$) and in the SO_4^{2-} ion ($\delta^{18}O_{SO_4}$), coupled to $\delta^{34}S_{SO_4}$, are used to partition the source of riverine SO_4^{2-}. The $\delta^{18}O_{SO_4}$ and $\delta^{34}S_{SO_4}$ of sedimentary sulfate minerals are relatively well constrained through geological time and show a narrow range, unlike the $\delta^{34}S_{SO_4}$ of pyrite (Claypool *et al.*, 1980; Thode, 1991). We argue that SO_4^{2-} derived from the oxidative weathering of pyrite has a $\delta^{18}O_{SO_4}$ predominantly reflecting local water ($\delta^{18}O_{H_2O}$) which can be determined at a catchment scale. These constraints are used to partition the fraction of dissolved SO_4^{2-} derived from the oxidative weathering of pyrite, with uncertainties estimated using a Monte-Carlo approach.

This method is applied to a new data-set from one of the world's largest river basins, the Mekong River in southeast Asia, which drains a diverse set of lithologies (with sulfide and sulfate rocks), topography, and climatic regimes. Whilst the SO_4^{2-} concentration in the Mekong River is low compared to many large rivers (mean value of ~90 μmol/L compared to ~118 μmol/L in the Ganges, for example, Li *et al.*, 2014; Bickle *et al.*, 2018), the high water discharge in the Mekong (470 km^3/yr cf. the Ganges with 377 km^3/yr) yields an equivalent SO_4^{2-} flux.

As such, the Mekong provides an ideal test basin to determine the significance of pyrite weathering in a continental scale catchment, with diverse mixtures of the two main riverine SO_4^{2-} sources, in contrast to the sulfide weathering-dominated basins on which most previous work has focused, such as the Mackenzie (Calmels *et al.*, 2007), the Amazonian headwaters (Torres *et al.*, 2016) or the Himalayas (Turchyn *et al.*, 2013).

We partition SO_4^{2-} in the Mekong between rain, pyrite and gypsum inputs and provide an illustration of the implications

for CO_2 consumption by silicate weathering on a previously published estimate of CO_2 consumption in the Mekong River. The results have clear implications for quantifying the carbon budget of global river systems and the impact of silicate weathering as a global climate moderator.

2. Materials and methods

2.1. Study area

The Mekong is the world's tenth largest river in terms of discharge (Dai & Trenberth, 2002), draining 795,000 km^2, passing though China, Myanmar, Laos, Thailand, Cambodia, and Vietnam (Fig. 2A). The hydrograph has a single peak flood pulse, typical of monsoonal rivers (Tipper *et al.*, 2006) and the climate is dominated by a wet season between June and November when there is a 20-fold increase in discharge (Mekong River Commission, 2016). The geology of the Mekong basin (Fig. 2B) is complex, diverse and poorly constrained (Chinese Academy of Geological Sciences, 1975; Gupta & Liew, 2007). Global lithological models suggest approximately 50% of the lithology is carbonate, mainly located in northern China and Laos (Amiotte Suchet *et al.*, 2003).

The Mekong headwaters are on the Tibetan Plateau (up to 5000 m.a.s.l.) flowing through the Eastern Syntaxis of the Himalaya, an area of steep topography, narrow gorges, and rapid exhumation (Lang *et al.*, 2016). The headwaters drain Palaeozoic–Triassic sedimentary rocks from the Qiangtang Block and clastic sedimentary rocks from the Mesozoic arc (Borges *et al.*, 2008). Whilst evaporite, clastic, and metamorphic rocks are present, carbonates dominate the Upper Mekong bedrock (Gupta & Liew, 2007; Wu *et al.*, 2008; Noh *et al.*, 2009; Jiang *et al.*, 2017). After exiting the Eastern Syntaxis, following a rapid decrease in altitude, the Mekong follows a distinct geological boundary. On the east bank (Laos) tributaries drain sheer–walled karst in the Annamite mountains comprising Carboniferous–Lower Permian Limestones and Jurassic-Cretaceous sandstones (Kiernan, 2015; Ponta & Aharon, 2014). Cretaceous intermediate-basic extrusive units are also found in northern Laos. On the west bank (Myanmar and Thailand), tributaries drain the Khorat Plateau which exposes epi-continental sediments deposited in restricted basins (Tabakh *et al.*, 1998, 1999).The lithology comprises fluvial and lacustrine facies and an extensive Late Cretaceous–early Tertiary evaporite succession, known as the Maha Sarakham Formation, formed by three major marine influx events (Tabakh *et al.*, 1998, 1999). In the lower reaches of the Mekong there are Mesozoic-Neogene basalts and Quaternary alluvium overlaying Jurassic and Triassic sedimentary units (Gupta & Liew, 2007). The Tonle Kong tributary, which joins the Mekong in northern Cambodia, flows over Proterozoic units and some small outcrops of Proterozoic granites (Chinese Academy of Geological Sciences, 1975).

2.2. Sample description

Mainstem and major tributaries of the Mekong river were sampled during the peak monsoon seasons of 2014, 2016, and 2017 (Fig. 2A). Rain-water samples were collected when meteorological conditions permitted. Where possible, instantaneous river discharge was measured by an acoustic Doppler current profiler (ADCP, Rio Grande II (1200 kHz), Teledyne Instruments) deployed from a moving boat. Surface waters were collected from the centre of the main channel and filtered within 6 hours through 142 mm 0.2 μm PES filters pre-cleaned by filtering 2.5 L of river water. Immediately after filtering, a subset (~2 L) of each sample was loaded on columns filled with 5 mL Dowex 1X8-200, 100-200 mesh, anion exchange resin to obtain >800 μg SO_4^{2-} needed for $\delta^{34}S_{SO_4}$ and $\delta^{18}O_{SO_4}$ analysis (Hindshaw *et al.*, 2016). The resin was pre-conditioned with 60 mL of 3M distilled HCl, then 60 mL of 18.2 MΩ H_2O. The SO_4^{2-} was stored on the resin and kept refrigerated until the time of sample preparation. Samples for cation analysis were collected into acid-cleaned HDPE bottles rinsed with filtered river water, then acidified to pH < 2 using distilled HNO_3. A separate non-acidified aliquot was collected for major anions and $\delta^{18}O_{H_2O}$ analysis in 18.2 MΩ H_2O-washed amber HDPE bottles. Total alkalinity

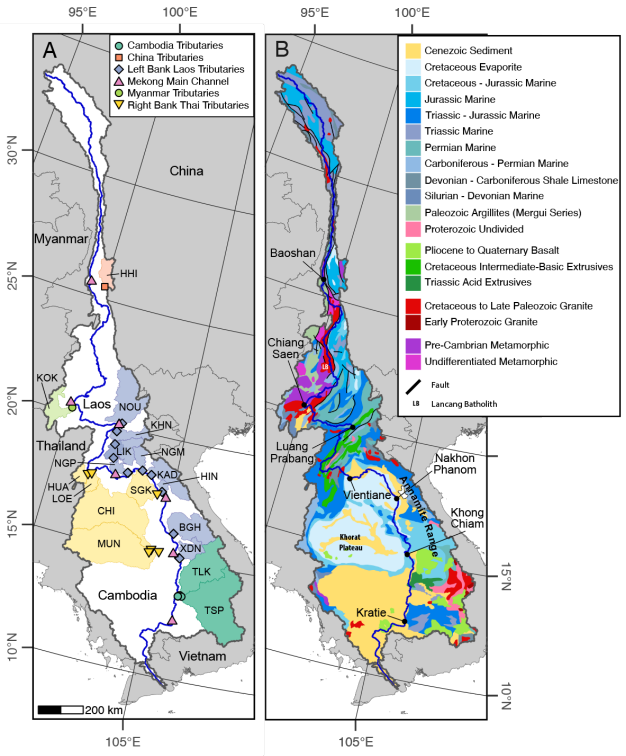

Figure 2: Maps of the Mekong river basin and its tributaries. A) Samples collected from the main stem at 5 locations (pink triangles): Baoshan, Luang Prabang, Vientiane, Pakse and Kratie and from 18 tributaries (coloured for country location, see legend): Heihui (HHI), Mae Kok (KOK), Hueang (HUA), Loei (LOE), Songkhram (SGK), Chi (CHI), Mun (MUN), Nam Ou (NOU), Nam Khan (KHN), Nam Lik (LIK), Nam Ngiep (NGP), Nam Ngjum (NGM), Nam Kading (KAD), Nam Hinboun (HIN), Xe Banghiang (BGH), Xe Don (XDN), Tonle Kong (TLK), Tonle Srepok (TSP). Chiang Saen, Nakhon Phanom, Khong Chiam are additional main stem sites where MRC data is available (Mekong River Commission, 2016). B) Geological map of the Mekong river basin, modified after Chinese Academy of Geological Sciences (1975).

was measured by Gran titration in the field with 0.05M HCl and used to verify charge balance.

2.3. Major ion concentrations

Major cation and total sulfur dissolved concentrations were measured by ICP-OES (Agilent 5100) at the Dept. Earth Sciences, University of Cambridge calibrated against synthetic standards spanning the concentration ranges of the samples (Table 1). Analyses of external standard reference materials SPS-SW2, SLRS-5 and SLRS-6 were within ± 5% of certified values (n=137, SI 3). Anions (Cl^-, SO_4^{2-}) were measured on a Thermo Dionex ICS-5000+ Ion Chromatograph. Repeated analyses of external standard LGC6025 River water were within ± 4% of certified values (n=85, SI 4).

2.4. S and O isotope analyses

Sulfate was eluted off the Dowex resin column with 20 mL 0.8M distilled HCl in a class 1000 clean laboratory, and mixed with $BaCl_2$ to precipitate barite ($BaSO_4$). The precipitate was subsequently cleaned with 6M HCl and rinsed three times with 18.2 MΩ H_2O. Other oxy-anions such as nitrate have greatly different oxygen isotope compositions and can be a source of contamination during barite precipitation (SI 2). To remove any impurities, the barite was dissolved in 10 mL 0.05M diethylenetriaminepentaacetic acid (DTPA), then slowly reprecipitated by lowering the solution pH to 3–4 (Bao, 2006). The barite was cleaned three times with 18.2 MΩ H_2O and dried at 70°C. The validation of the purification methodology and theoretical effects of contamination are demonstrated in SI 2.

Stable isotope ratios $\delta^{18}O_{SO_4}$ and $\delta^{34}S_{SO_4}$ for dissolved SO_4^{2-} were analysed using gas source isotope ratio mass spectrometers (GS-IRMS) in the Godwin Laboratory, University of Cambridge (Rennie & Turchyn, 2014). For $\delta^{18}O_{SO_4}$ analysis, 180 μg of the barite was pyrolysed in a thermal conversion element analyser (TC/EA) and passed via continuous He flow into a Thermo Delta V mass spectrometer via a ConFlo 3. The $\delta^{18}O_{SO_4}$ isotope measurements were calibrated to V-SMOW via the reference gas analysis. Samples were run in quadruplicate and the data in Table 1 are an average of these replicates. For $\delta^{34}S_{SO_4}$ analysis, 400 μg of barite was combusted in excess oxygen with vanadium pentoxide in a Flash EA coupled via continuous flow and analysed by a Thermo Delta V Mass spectrometer. Both $\delta^{34}S_{SO_4}$ and $\delta^{18}O_{SO_4}$ were normalised to NBS 127 ($\delta^{34}S_{SO_4}$ = 21.1‰, $\delta^{18}O_{SO_4}$ = 8.6‰), which were used to correct for machine drift and absolute offset. The overall analytical precision was better than 0.3‰ 1σ for $\delta^{18}O_{SO_4}$ (n=22) and 0.09‰ 1σ for $\delta^{34}S_{SO_4}$ (n=39). External standards IAEA SO-5 and IAEA SO-6 were precise to within 0.13‰ for $\delta^{18}O_{SO_4}$ (1σ, n=12) and 0.19‰ for $\delta^{34}S_{SO_4}$ (1σ, n=6). Two full replicates of the entire method were made using OSIL IAPSO Atlantic Seawater resulting in values within error of standard seawater values ($\delta^{34}S$ = 20.94‰ ± 0.09 1σ, $\delta^{18}O_{SO_4}$ = 8.3‰ ± 0.2 1σ).

Cavity ring down mass spectrometry (Picarro L1102-i interfaced with a A0211 high-precision vaporizer) was used to determine $\delta^{18}O_{H_2O}$ (Turchyn *et al.*, 2013). Samples were calibrated against JRW, SPIT and BOTTY standards and results are expressed relative to V-SMOW in parts per thousand. Repeat measurements of the standards had a precision of $\delta^{18}O_{H_2O}$ = 0.1‰ 2σ (n=28).

3. Results

Concentrations for selected elements, $\delta^{18}O_{H_2O}$, $\delta^{34}S_{SO_4}$ and $\delta^{18}O_{SO_4}$ for selected samples are given in Table 1 with additional major element data (e.g., tributaries and rain) in Table S5. Discharge determined by ADCP are provided for selected samples. Discharge increases consistently downstream from ~1700 m^3s^{-1} in the northern most main river sample, to > 35,000m^3s^{-1} at Kratie, close to the mouth (Fig. 3A). Discharge was determined by ADCP for 4 of the tributaries, and historical discharge data is available for 10 tributaries in addition to 6 sites on the main river (Mekong River Commission, 2016).

3.1. Major solutes

The Mekong and its tributaries show a very wide range in SO_4^{2-} concentrations from 4 to 705 μmol/L, with an average mainstem value of 129 μmol/L, 2.6 times more dilute than the global river average (332 μmol/L, Burke *et al.*, 2018). Main channel SO_4^{2-} concentrations decrease downstream from 705 to 39 μmol/L as the discharge increases. Data from 2014, 2016 and 2017 are consistent with a historical data set from the Mekong River Commission (1985-2000; Mekong River Commission, 2016; Li *et al.*, 2014). Tributary concentrations are mainly lower than the mainstem with two notable exceptions, the Nam Lik and the Loei (Fig. 3B), similar to previously published values (Wu *et al.*, 2008; Noh *et al.*, 2009; Mekong River Commission, 2016). Concentrations of Cl^- range from < 5 μmol/L to 816 μmol/L. The high concentrations are suggestive of halite dissolution, with concentrations greater than 376 μmol/L delivered by west bank (Thai) tributaries draining the evaporite-rich Khorat Plateau (Fig. 3C). The high Cl^- concentrations in these tributaries are not matched by significantly higher Ca^{2+} or SO_4^{2-} concentrations (Fig. 3B, C, D). The tributaries with the lowest Cl^- are lower than that of the sampled rain.

3.2. Oxygen and sulfur isotopic ratios

There is a large range in $\delta^{18}O_{H_2O}$ from -16.4‰ to -7.4‰, consistent with the Global Network for Isotopes in Precipitation (GNIP) model (Fig. S3, Terzer *et al.*, 2013) with the largest change associated with the decrease in altitude across the eastern Himalayan syntaxis.

Tributary $\delta^{18}O_{SO_4}$ values range from -0.3‰ to +12.0‰ (Fig. 3F), a greater range than $\delta^{18}O_{H_2O}$. Mainstem samples have a smaller $\delta^{18}O_{SO_4}$ range of 5.5‰ with the lowest values in the headwaters (-0.3‰) and the highest values closer to the mouth (5.2‰).

The difference between oxygen isotope compositions in SO_4^{2-} and H_2O, $\Delta^{18}O_{SO_4-H_2O}$, is a function of the fraction

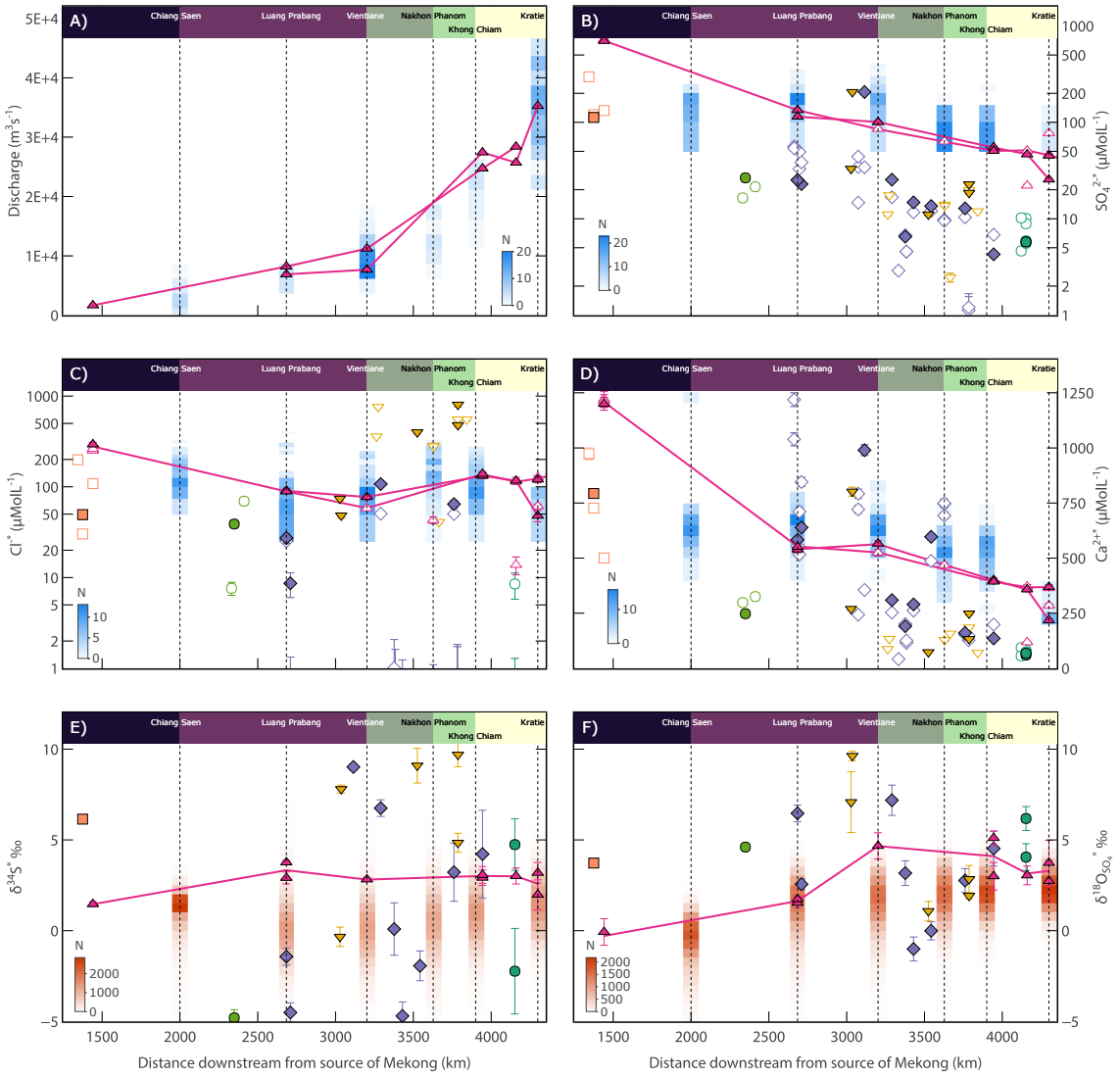

Figure 3: Downstream variations in discharge and dissolved solutes SO_4^{2-}, Cl^- and Ca^{2+} and $\delta^{34}S_{SO_4}$ and $\delta^{18}O_{SO_4}$. Data is corrected for rain inputs (Section 4.1) with 2σ uncertainties smaller than the symbols, if not shown. Distance downstream is sectioned by mainstem monitoring stations (Fig. 2A). Mainstem samples highlighted by pink line (each line is unique for a single year). Filled symbols represent samples where $\delta^{34}S_{SO_4}$ and $\delta^{18}O_{SO_4}$ were measured; open symbols only have major solutes. The blue coloured shading represents a heat map of the 1985-2000 data set (Mekong River Commission, 2016) for September; a brighter colour indicating a greater number of counts. The red shaded data is a heatmap of modelled output from the downstream mixing model (Section 5.4).

of oxygen derived from water that contributes to the SO_4^{2-} molecule, compared to other sources, such as molecular oxygen or the dissolution of sedimentary sulfates (discussed in detail in Section 4.3). In the Mekong, $\Delta^{18}O_{SO_4-H_2O}$ ranges from 8.3‰ to 20.7‰ and spans the $\Delta^{18}O_{SO_4-H_2O}$ (and $\delta^{34}S$) range of many global rivers (Fig. 4).

The mainstem shows a small downstream increase of $\delta^{34}S_{SO_4}$ values from 1.50‰ to 3.87‰ (Fig. 3E). The tributaries however show a ~13.5‰ range (-3.46‰ to +10.04‰), scattering to values greater and lower than the main river. The lowest $\delta^{34}S_{SO_4}$ values are from tributaries that drain northeast Myanmar and catchments in northern Laos whilst the highest $\delta^{34}S_{SO_4}$ values are from catchments in northeastern Thailand. Despite the significant variability in the tributaries, samples collected in 2016 and 2017 from mainstem sites at Luang Prabang, Pakse and Kratie have a limited inter-annual variability of 0.6‰ 1σ and 1.4‰ 1σ for $\delta^{34}S_{SO_4}$ and $\delta^{18}O_{SO_4}$ values, respectively, suggesting that relative inputs vary little from year to year.

4. Sources of Sulfate to River Waters

The most significant sources of riverine SO_4^{2-} are the dissolution of sedimentary sulfate minerals such as gypsum ($CaSO_4{\cdot}2H_2O$), anhydrite ($CaSO_4$) and the oxidative weathering of sedimentary sulfide minerals such as pyrite (FeS_2). Possible additional inputs are from volcanic emissions, magmatic sulfide, carbonate associated SO_4^{2-}, rain and anthropogenic pollution from fertilisers, industrial waste water and coal burning (Robinson & Bottrell, 1997; Canfield, 2004).

Table 1: Major cations and anions and stable isotope ratio data for main stem and tributaries. Missing main stem f_{pyr} values are due to insufficient SO_4^{2-} concentration or discharge data to calculate f_{pyr} using mass balance (Section 5.4). **Indicates discharge from (Mekong River Commission, 2016). SPM= suspended particulate matter and where possible are the mean values of multiple samples collected at different depths in the water column. Min and Max $\delta^{18}O_{GNIP}$ correspond to the 25th and 75th percentiles of the rain weighted GNIP model as described in the text. D/S = Downstream, U/S = Upstream, n.d. = no data or no sample collected.

ID	Group	River	Date	Basin area	Distance from source	N	E	Discharge	SPM	T	pH	Ca^{2+}	Mg^{2+}	K^+	Na^+	Cl^-	SO_4^{2-}	NO_3^-	HCO_3^-	$\delta^{18}O_{H_2O}$	$\delta^{18}O_{SO_4}$	$\delta^{34}S_{SO_4}$	$\delta^{18}O_{GNIP}$		$\delta^{34}S_{pyr}$	f_{rain}	f_{pyr}	f_{gyp}
				km^2	km	°	°	m^3/s	mg/L	°C		μmol/L								± 2σ	± 1σ	± 1σ	min	max	±1σ	±1σ	±1σ	±1σ
MEK16-112	Cambodia	Tonle Srepok	2016-09-20	50202	4152	13.547	106.04	5585	n.d.	27.8	7.02	67.6	48.3	29.0	78.3	18.4	8.21	2.64	295	-8.7 ± 0.1	6.5 ± 0.3	2.1 ± 0.1	-7.8	-6.1	-21 ± 10	0.30 ± 0.04	0.53 ± 0.12	0.47 ± 0.12
MEK16-119	Cambodia	Tonle Kong	2016-09-20	28792	4152	13.559	106.04	n.d.		28.2	7.08	73.2	47.9	22.6	67.3	12.6	7.42	2.43	291	-8.3 ± 0.1	4.7 ± 0.4	6.7 ± 0.1	-8.2	-6.3	-1 ± 4	0.23 ± 0.03	0.64 ± 0.11	0.36 ± 0.11
MEK17-123	China	Heihui	2017-09-15	7284	1375	25.514	99.993	n.d.	1635	21.8	8.15	799	246	35.4	176	61.2	114	28.1	1860	-12.9 ± 0.1	3.8 ± 0.1	6.3 ± 0.2	-14.1	-9.0	-2 ± 4	0.02 ± <0.01	0.54 ± 0.10	0.46 ± 0.10
MEK16-012	Left	Nam Khan	2016-09-12	7472	2710	19.766	102.18	n.d.		23.7	7.97	644	201	45.0	165	20.4	25.2	6.04	1800	-9.3 ± 0.1	3.0 ± 0.3	-2.9 ± 0.1	-10.5	-5.8	-14 ± 5	0.09 ± 0.01	0.69 ± 0.10	0.31 ± 0.10
MEK16-047	Left	Nam Ngiap	2016-09-15	4515	3376	18.417	103.60	544**	n.d.	25.4	7.42	196	75.5	19.5	75.5	9.32	8.35	1.65	609	-8.9 ± 0.0	4.1 ± 0.4	2.7 ± 0.1	-10.0	-5.8	-9 ± 5	0.22 ± 0.03	0.66 ± 0.11	0.34 ± 0.11
MEK16-051	Left	Nam Kading	2016-09-15	14807	3430	18.324	104.00	524**	n.d.	26.4	7.85	296	58.4	14.3	41.8	11.1	16.9	5.18	725	-8.3 ± 0.1	0.0 ± 0.6	-2.5 ± 0.1	-9.7	-6.5	-9 ± 3	0.12 ± 0.02	0.84 ± 0.08	0.16 ± 0.08
MEK16-053	Left	Nam Hinboun	2016-09-15	2212	3543	17.727	104.57	n.d.		26.5	7.56	602	86.5	10.9	32.8	10.7	15.6	1.42	1350	-8.4 ± 0.0	0.9 ± 0.4	0.1 ± 0.1	-9.1	-6.6	-6 ± 3	0.13 ± 0.02	0.81 ± 0.08	0.19 ± 0.08
MEK16-077	Left	Xe Banghiang	2016-09-17	19978	3761	16.098	105.38	845**	n.d.	28.4	7.13	171	68.2	31.0	124	91.3	16.4	12.0	482	-9.2 ± 0.1	3.8 ± 0.4	5.5 ± 0.3	-8.5	-6.4	-2 ± 4	0.22 ± 0.02	0.69 ± 0.10	0.31 ± 0.10
MEK16-087	Left	Xe Don	2016-09-18	7348	3944	15.133	105.81	666	n.d.	30.0	7.44	141	94.5	20.8	96.4	14.9	6.31	1.51	592	-9.0 ± 0.0	5.4 ± 0.5	7.0 ± 0.1	-8.4	-6.4	-3 ± 6	0.32 ± 0.05	0.61 ± 0.12	0.39 ± 0.12
MEK17-127	Left	Nam Ou	2017-09-17	26058	2684	20.115	102.29	713	120	26.0	8.20	585	174	24.6	157	39.1	27.3	NA	1520	-8.9 ± 0.1	6.5 ± 0.4	-0.2 ± 0.1	-10.6	-5.4	-21 ± 10	0.08 ± 0.01	0.49 ± 0.12	0.51 ± 0.12
MEK17-146	Left	Nam Lik	2017-09-18	5258	3115	19.216	102.24	n.d.	3886	27.6	7.96	996	318	17.6	140	7.91	208	NA	2210	-8.8 ± 0.1	11.9 ± 0.3	9.1 ± 0.2	-9.3	-5.8	-24 ± 22	0.01 ± <0.01	0.19 ± 0.08	0.81 ± 0.08
MEK17-158	Left	Nam Ngjum	2017-09-20	16347	3290	18.180	103.04	950**	n.d.	28.2	7.04	316	112	18.6	166	119	27.8	1.52	814	-8.3 ± 0.1	7.2 ± 0.9	7.3 ± 0.1	-9.5	-5.8	-6 ± 9	0.08 ± 0.01	0.44 ± 0.13	0.56 ± 0.13
MEK17-230	Myanmar	Mae Kok	2017-10-02	10633	2349	20.228	100.13	243**	273	27.8	7.19	254	125	57.6	160	50.6	28.9	NA	760	-8.6 ± 0.1	4.8 ± 0.0	-3.5 ± 0.0	-9.1	-5.3	-19 ± 6	0.08 ± 0.01	0.61 ± 0.11	0.39 ± 0.11
MEK17-236	Right	Hueang	2017-10-04	4815	3028	17.730	101.49	n.d.	3284	25.6	7.36	276	121	47.0	235	85.4	35.2	NA	825	-10.2 ± 0.1	7.1 ± 1.5	0.5 ± 0.3	-8.5	-5.2	-21 ± 14	0.06 ± 0.01	0.47 ± 0.14	0.53 ± 0.14
MEK17-240	Right	Loei	2017-10-04	3954	3037	17.803	101.63	n.d.	115	28.1	7.81	808	234	52.0	307	60.4	208	NA	1800	-9.0 ± 0.1	9.6 ± 0.3	7.9 ± 0.2	-8.3	-5.4	-12 ± 14	0.01 ± <0.01	0.31 ± 0.10	0.69 ± 0.10
MEK17-245	Right	Songkhram	2017-10-05	12987	3525	17.611	104.40	n.d.		31.0	6.29	79.2	44.8	40.3	386	412	13.3	NA	211	-9.1 ± 0.1	2.2 ± 0.4	9.9 ± 0.1	-7.9	-6.2	7 ± 2	0.17 ± 0.02	0.78 ± 0.09	0.22 ± 0.09
MEK17-256	Right	Chi	2017-10-06	49402	3786	15.266	104.64	614**	59	32.2	6.96	254	93.4	63.4	557	489	25.0	7.01	706	-7.7 ± 0.1	2.4 ± 0.1	5.6 ± 0.1	-8.1	-5.5	1 ± 2	0.09 ± 0.01	0.75 ± 0.09	0.25 ± 0.09
MEK17-257	Right	Mun U/S	2017-10-06	53397	3787	15.143	104.58	1790**	n.d.	30.5	6.45	139	63.5	42.3	781	816	20.8	NA	376	-7.4 ± 0.1	3.4 ± 0.6	10.0 ± 0.3	-7.6	-5.5	7 ± 2	0.11 ± 0.01	0.71 ± 0.10	0.29 ± 0.10
MEK17-107	Main	Baoshan	2017-09-12	92639	1441	25.432	99.342	1656	158	19.7	8.41	1210	556	45.1	497	305	705	19.4	2200	-16.4 ± 0.1	-0.3 ± 0.8	1.5 ± 0.1	-16.2	-12.0	-6 ± 3	0.00 ± <0.01	0.66 ± 0.10	0.34 ± 0.10
MEK16-007	Main	Vientiane	2016-09-11	305128	3202	17.963	102.57	7666	n.d.	27.4	6.39	572	186	38.1	218	89.2	103	1.44	1410	-9.2 ± 0.1	4.7 ± 0.6	3.0 ± 0.0	n.d.		n.d.	0.02 ± <0.01	n.d.	n.d.
MEK16-033	Main	Luang Prabang	2016-09-13	231768	2684	20.057	102.20	6881	n.d.	26.4	7.90	546	186	40.8	225	102	117	1.40	1390	-9.6 ± 0.1	1.6 ± 0.3	3.9 ± 0.0	n.d.		n.d.	0.02 ± <0.01	n.d.	n.d.
MEK16-096	Main	Pakse	2016-09-18	542799	3944	15.119	105.78	27430	n.d.	28.2	7.55	412	128	33.5	222	160	58.6	1.95	1040	-8.5 ± 0.1	5.3 ± 0.4	3.6 ± 0.2	n.d.	n.d.	n.d.	0.06 ± 0.01	n.d.	n.d.
MEK16-106	Main	Stung Treng	2016-09-19	561329	4160	13.544	105.96	25704	n.d.	29.0	7.52	369	115	32.1	203	144	50.3	4.06	930	-8.5 ± 0.1	3.4 ± 0.4	3.7 ± 0.2	n.d.		n.d.	0.07 ± 0.01	n.d.	n.d.
MEK16-137	Main	Kratie	2016-09-22	652181	4299	12.469	106.02	35253	n.d.	29.5	7.68	229	86.0	29.5	136	75.5	29.2	1.44	635	-8.6 ± 0.1	4.1 ± 1.1	3.3 ± 0.3	n.d.		n.d.	0.12 ± 0.01	n.d.	n.d.
MEK17-135	Main	Luang Prabang	2017-09-17	231768	2684	20.056	102.20	8204	852	26.2	7.87	559	200	45.5	208	101	136	14.6	1310	-10.3 ± 0.1	1.8 ± 0.1	3.1 ± 0.3	n.d.		n.d.	0.02 ± <0.01	n.d.	n.d.
MEK17-189	Main	Pakse	2017-09-22	542799	3944	15.118	105.78	24722	910	28.8	7.15	405	136	36.1	192	165	54.2	5.49	958	-9.9 ± 0.1	3.3 ± 0.8	3.8 ± 0.3	n.d.		n.d.	0.07 ± 0.01	n.d.	n.d.
MEK17-213	Main	Kratie	2017-09-25	652181	4299	12.459	106.02	33155	251	28.9	7.18	381	130	37.2	207	148	48.5	13.8	896	-9.6 ± 0.1	3.0 ± 1.1	3.9 ± 0.3	n.d.		n.d.	0.07 ± 0.01	n.d.	n.d.

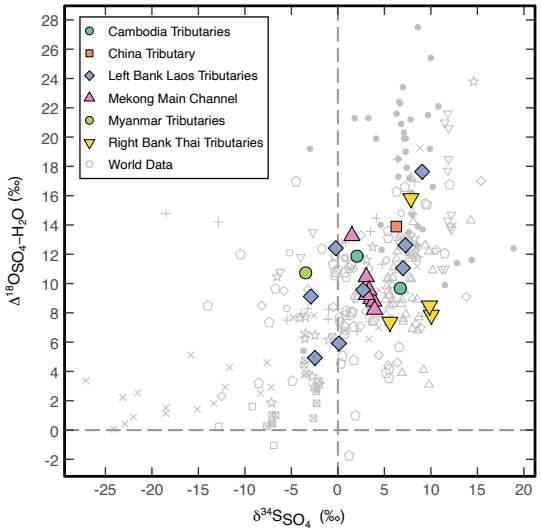

Figure 4: Sulfur and oxygen isotope compositions measured in dissolved SO_4^{2-} and H_2O of the Mekong River and its tributaries compared to global data (grey open symbols, symbols correspond to Fig. 1). Error bars are smaller than symbols for Mekong data.

4.1. Atmospheric Sulfate Inputs

Atmospheric inputs were corrected for using the SO_4^{2-}/Cl^- ratio in the rain:

$$[SO_4^{2-}]^* = [SO_{4_{river}}^{2-}] - [Cl^-_{rain}] \cdot \left(\frac{[SO_4^{2-}]}{[Cl^-]} \right)_{rain} \quad (2)$$

This does not account for evapotranspiration because the high Cl^- content in four of the tributaries (> 300 μmol/L) suggests that a significant proportion of the Cl^- budget is derived from halite weathering rather than rain inputs alone. Of the 18 tributaries with $\delta^{34}S_{SO_4}$ and $\delta^{18}O_{SO_4}$ data, 8 have chloride concentrations lower than that of the rain, suggesting that evapo-transpiration has not influenced the data to an appreciable degree. Therefore it was assumed that the chloride contribution from rain cannot exceed the chloride concentration of the river such that:

$$[Cl^-_{river}]^* = ([Cl^-_{river}] - [Cl^-_{rain}]) \geq 0 \quad (3)$$

The three rain samples (Table S5), have molar SO_4^{2-}/Cl^- ratio ranges between 0.12 and 0.19. The river water samples were corrected using the rain composition of closest geographical proximity. The rain correction for SO_4^{2-} ranges between < 1% in the concentrated samples to 30% in the more dilute samples (Fig. S2].

Atmospheric inputs could have a significant impact on the $\delta^{34}S_{SO_4}$ and $\delta^{18}O_{SO_4}$ of the river waters, especially in dilute samples where up to 30% of SO_4^{2-} is derived from rain. The rain samples collected were too small to enable measurement of $\delta^{34}S_{SO_4}$ and $\delta^{18}O_{SO_4}$ values. Instead it was assumed that the rain $\delta^{34}S_{SO_4}$ and $\delta^{18}O_{SO_4}$ falls between that of seawater (21‰ and 9.3‰ respectively, sources in Table S1) and the average of the most dilute tributaries with the greatest rain contribution (SO_4^{2-} < 15 and Cl^- < 18 μmol/L, and $\delta^{34}S_{SO_4}$ and $\delta^{18}O_{SO_4}$ of 4.62 and 5.19‰ respectively). This range of $\delta^{34}S_{SO_4}$ values is significantly wider than that observed in Chinese Rivers (Han *et al.*, 2016) and similar to that observed for $\delta^{18}O_{SO_4}$ values in rain. The river waters were corrected for rain inputs using the mass balance equation:

$$\delta^* = \frac{\delta_{river} \cdot [SO_{4_{river}}^{2-}] - \delta_{rain} \cdot ([SO_{4_{river}}^{2-}] - [SO_4^{2-}]^*)}{[SO_4^{2-}]^*} \quad (4)$$

where δ refers to either $\delta^{34}S_{SO_4}$ and $\delta^{18}O_{SO_4}$ and δ^* denotes corrected values. The maximum rain correction is 4.7‰ and 1.04‰ for $\delta^{34}S_{SO_4}$ and $\delta^{18}O_{SO_4}$ values respectively (Fig. S2). The uncertainty on the rain correction was estimated using a Monte-Carlo simulation with an assumed 2.5% and 10% 1σ uncertainty (normal distribution) on the elemental concentrations of river and rain water respectively. For the uncertainty on $\delta^{34}S_{SO_4}$ and $\delta^{18}O_{SO_4}$ in rain waters, 10,000 values were randomly sampled from a uniform distribution between the rain end-member $\delta^{34}S_{SO_4}$ and $\delta^{18}O_{SO_4}$ values and propagated through Eqns. 2-4. This amplifies the analytical uncertainties of < 0.3‰ for $\delta^{34}S_{SO_4}$ and $\delta^{18}O_{SO_4}$, to a maximum of 2.3‰ and 1.6‰ 1σ for $\delta^{34}S_{SO_4}{}^*$ and $\delta^{18}O_{SO_4}{}^*$ respectively.

4.2. Sedimentary Sulfate Mineral Inputs

Significant quantities of SO_4^{2-} remain after correcting for rain, suggesting that sedimentary sulfate and/or sulfide inputs are important in the Mekong Basin. Sedimentary sulfate deposits are documented within the Khorat Plateau in the Mekong River basin. Anhydrite beds and nodules contained within halite have $\delta^{34}S$ values ranging from +6.4 to 17.7‰ with a mean value of 15.1‰ (Pisutha-Arnond *et al.*, 1986; Tabakh *et al.*, 1998, 1999). Whilst the range in $\delta^{34}S$ values is quite large, the range in $\delta^{18}O_{SO_4}$ values is much narrower in the anhydrite beds; between +11.0 to +14.2‰ (Pisutha-Arnond *et al.*, 1986), well within the Phanerozoic range of $\delta^{18}O_{SO_4}$ (~10‰ (Crockford *et al.*, 2019).

4.3. Sedimentary Sulfide Mineral Inputs

The supply of SO_4^{2-} to the hydrosphere from the oxidative weathering of pyrite is controlled via two main reaction pathways, involving either molecular O_2 or water combined with the reduction of Fe^{3+} in the critical zone environment. Whilst the resulting $\delta^{34}S_{SO_4}$ is inherited from the composition of the pyrite, the $\delta^{18}O_{SO_4}$ is controlled by the source of the oxygen (with differing $\delta^{18}O$), in addition to fractionation factors between SO_4^{2-} and molecular or water oxygen ($\varepsilon_{SO_4-O_2}$ and $\varepsilon_{SO_4-H_2O}$). For the kinetically faster, bacterially mediated reaction pathway, oxygen in the SO_4^{2-} molecule is quantitatively derived from water (Balci *et al.*, 2007):

$$FeS_2 + 14Fe^{3+} + 8H_2O \rightarrow 15Fe^{2+} + 2SO_4^{2-} + 16H^+ \quad (5)$$

This reaction occurs in anoxic environments via the reduction of ferric iron (Fe^{3+}, van Everdingen & Krouse, 1985; Calmels *et al.*, 2007).

Table 2: Definition, values and distributions of assumed end-member isotopic compositions, fractionation factors, elemental concentrations and f_{O_2} used in calculations of the rain correction and partitioning of the fraction of sulfate derived from pyrite and gypsum. Uncertainties of the calculated parameters were estimated by randomly sampling each parameter 10,000 times (Monte Carlo) within the listed distributions and repeating the calculations for each tributary. GNIP 25th and GNIP 75th refer to the percentiles from the the rain weighted GNIP $\delta^{18}O$ precipitation model (Fig S4). * refers to the fact that the maximum possible $\delta^{18}O_{O_2}$ of molecular O_2 incorporated into the SO_4^{2-} molecule is a function of f_{O_2} (Fig. S7).

Parameter		If normal distribution		If uniform distribution	
		Value	1σ	Min value	Max value
$\delta^{18}O_{SO_4\ gyp}$	Oxygen isotope ratio of gypsum end-member	14.5‰	2‰		
$\delta^{34}S_{SO_4\ gyp}$	Sulfur isotope ratio of gypsum end-member	15.1‰	2.1‰		
$\delta^{18}O_{O_2}$	molecular O_2			23‰	70‰*
$\varepsilon_{SO_4-H_2O}$	Fractionation factor for $\delta^{18}O$ between H_2O and SO_4^{2-}			0‰	4‰
$\varepsilon_{SO_4-O_2}$	Fractionation factor for $\delta^{18}O$ between molecular O_2 and SO_4^{2-}			-12.1‰	-8.1‰
f_{O_2}	Fraction of O_2 in dissolved SO_4^{2-} derived from atmospheric O_2, $f_{O_2} + f_{H_2O} = 1$			0%	17%*
$\delta^{18}O_{H_2O}$	Oxygen isotope composition of water at the time SO_4^{2-} molecule was formed			GNIP 25th	GNIP75th
$SO_{4\,river}^{2+}$	Measured sulfate concentration in the river	Measured	±2.5%		
Cl_{river}^{-}	Measured chloride concentration in the river	Measured	±2.5%		
$SO_{4\,rain}^{2+}$	Measured sulfate concentration in the rain	Measured	±10%		
Cl_{rain}^{-}	Measured chloride concentration in the rain	Measured	±10%		
$\delta^{18}O_{SO_4\,rain}$	Estimated $\delta^{18}O_{SO_4}$ for rain water			4.62‰	21‰
$\delta^{34}S_{SO_4\,rain}$	Estimated $\delta^{34}S_{SO_4}$ for rain water			5.19‰	9.3‰
$\delta^{18}O_{SO_4}{}^{*}$	Rain corrected $\delta^{18}O_{SO_4}$	Calculated			
$\delta^{34}S_{SO_4}{}^{*}$	Rain corrected $\delta^{34}S_{SO_4}$	Calculated			
$\delta^{34}S_{SO_4\ pyr}$	Estimated $\delta^{34}S$ of pyrite derived SO_4^{2-}	Calculated			

This net reaction is a simplification of the multiple step oxidation process (SI 8), but importantly the oxygen in the SO_4^{2-} is derived entirely from water within the critical zone. The $\delta^{18}O_{H_2O}$ that participates in the oxidation process can therefore be approximated by the $\delta^{18}O_{H_2O}$ of the river water sample itself, depending on the catchment size and the temporal and spatial variability of $\delta^{18}O_{H_2O}$ across the catchment (addressed in detail in section 4.4). Oxygen from water is incorporated into the SO_4^{2-} molecule with a fractionation factor ($\varepsilon_{SO_4-H_2O}$). Balci *et al.* (2007) and references therein estimated $\varepsilon_{SO_4-H_2O}$ to range from 0‰ to 4‰ depending on the metal (e.g., Fe^{3+}) used in the sulfide oxidation pathway.

Pyrite can additionally be oxidised aerobically, incorporating molecular O_2 into the SO_4^{2-} molecule (SI 9, van Everdingen & Krouse, 1985; Calmels *et al.*, 2007) following the reaction:

$$FeS_2 + \frac{7}{2}O_2 + H_2O \rightarrow Fe^{2+} + 2SO_4^{2-} + 2H^+ \qquad (6)$$

where oxygen within the SO_4^{2-} molecule is derived from both the atmosphere and local water. Although the reaction stoichiometry would suggest that oxygen is incorporated into the SO_4^{2-} molecule in the proportion 87.5:12.5 atmosphere:water (Taylor *et al.*, 1984a), experimental work has demonstrated persuasively that even in the presence of atmospheric oxygen, the majority of the oxygen in the SO_4^{2-} molecule is still derived from the water (Balci *et al.*, 2007). This is likely because the oxidation process of sulfide to SO_4^{2-} involves a number of intermediate steps (SI 8, Balci *et al.*, 2007). In laboratory settings a maximum of 17% atmospheric O_2 was incorporated into the SO_4^{2-} molecule (Balci *et al.*, 2007), a fraction which decreased as the reaction progresses.

Some studies have highlighted the dominance of the aerobic oxidation pathway for pyrite oxidation (e.g., Gu *et al.*, 2020) but in rapidly eroding Himalayan catchments (similar conditions to the Mekong Basin) $\Delta'^{17}O$ measurements have shown that most of the oxygen incorporated into the SO_4^{2-} molecule during pyrite oxidation is derived from meteoric water rather than molecular O_2 (Hemingway *et al.*, 2020). It is therefore likely that 17% represents an upper threshold for incorporation of molecular O_2 into SO_4^{2-}.

The $\delta^{18}O$ of atmospheric O_2 is well constrained at 23‰ (Kroopnick & Craig, 1972), however, molecular O_2 in the critical zone can be fractionated. Kim *et al.* (2017) reported $\delta^{18}O_{O_2}$ values as high as +70‰ (although mean values of the most oxygen-depleted samples were +62‰ and +40‰) in weathering profiles in very slowly eroding catchments. The most fractionated oxygen isotope ratios were observed when clay sealed the profile and the partial pressure of oxygen was reduced by oxidation of Fe^{2+} in clay minerals. Other studies have noted much less extreme oxygen isotope fractionations: Angert *et al.* (2001) recorded fractionations of < 2‰ as the O_2 content reduced to < 5% in soil profiles of approximately 1m thickness. To represent the maximum uncertainty, the full range of values for $\delta^{18}O_{O_2}$ between +23‰ and +70‰ (Table 2) was allowed for in the modelling. In addition to potentially variable $\delta^{18}O$ of molecular O_2, there is a fractionation factor between molecular O_2 and the SO_4^{2-} molecule ($\varepsilon_{SO_4-O_2}$) that has been determined experimentally to have a value of approximately -10.1‰ (Taylor *et al.*, 1984b; Balci *et al.*, 2007) and a uniform distribution of values between -8.1‰ and -12.1‰ was assumed in the modelling below.

The oxygen isotopic composition of the pyrite-derived SO_4^{2-} ($\delta^{18}O_{SO_4\ pyr}$) is therefore a function of 1) the fraction of water (f_{H_2O}) versus molecular O_2 (f_{O_2}) contributing oxygen atoms, 2) $\delta^{18}O_{H_2O}$ and $\delta^{18}O_{O_2}$ and 3) the fractionation factors between these phases and the SO_4^{2-} molecule ($\varepsilon_{SO_4-O_2}$ and $\varepsilon_{SO_4-H_2O}$) and

can be determined by the following mixing equation:

$$\delta^{18}O_{SO_4\ pyr} = f_{O_2}\left(\delta^{18}O_{O_2} + \varepsilon_{SO_4-O_2}\right) + f_{H_2O}\left(\delta^{18}O_{H_2O} + \varepsilon_{SO_4-H_2O}\right) \quad (7)$$

where:

$$f_{O_2} + f_{H_2O} = 1 \quad (8)$$

The fractional inputs of atmospheric and meteoric water oxygen, f_{O_2} and f_{H_2O}, respectively, depend on the reaction pathway of sulfide oxidation (Eqn. 5 or 6), and $\delta^{18}O_{H_2O}$ is the composition of the local water. The fractionation factors between oxygen and SO_4^{2-} ($\varepsilon_{SO_4-O_2}$) and water and SO_4^{2-} ($\varepsilon_{SO_4-H_2O}$), are given in Table 2.

This oxygen isotope mass balance (Eqn. 7) provides an important constraint on the maximum $\delta^{18}O_{O_2}$ and the maximum fraction of molecular O_2 (f_{O_2}) within the rapidly eroding setting of the Mekong Basin because $\delta^{18}O_{SO_4\ pyr}$ cannot exceed $\delta^{18}O_{SO_4}{}^*$ ($\delta^{18}O_{SO_4\ pyr} \leq \delta^{18}O_{SO_4}{}^*$). In the limiting case where $\delta^{18}O_{SO_4\ pyr} = \delta^{18}O_{SO_4}{}^*$ (where 100% of the riverine SO_4^{2-} is derived from pyrite oxidation), the maximum value of $\delta^{18}O_{O_2}$ is a function of the maximum value of f_{O_2}. This function (Eqn. S7) is illustrated for each tributary in Fig. S7 demonstrating that if very fractionated oxygen isotope ratios occur in the critical zone, the maximum possible f_{O_2} is significantly lowered in some tributaries such as the Kading or Hinboun (KAD and HIN). For most catchments however, $\delta^{18}O_{O_2}$ values anywhere between 23‰ and 70‰ are plausible with mass balance. In the tributaries where Eqn. S7 limits $\delta^{18}O_{O_2}$ and/or f_{O_2}, only a permissible range was taken to be used in Eqn. 7.

4.4. Spatial and temporal changes in the $\delta^{18}O$ of water in tributaries

Although $\delta^{18}O_{H_2O}$ measurements are made to a high precision, they may not accurately reflect the $\delta^{18}O_{H_2O}$ at the time or place the SO_4^{2-} molecule was formed because of spatial and temporal variability in $\delta^{18}O_{H_2O}$ across each of the tributary basins. The basin size ranges from 2000 to 93,000 km^2, with a maximum interquartile range in altitude of < 900m within a tributary basin, which will contribute a range of $\delta^{18}O_{H_2O}$ water values depending on exactly where and when the SO_4^{2-} molecule was formed. The tributary $\delta^{18}O_{H_2O}$ compares well to the GNIP model (Terzer *et al.*, 2013). The uncertainty on tributary $\delta^{18}O_{H_2O}$ (because of spatial and temporal variability) was determined by extracting the monthly GNIP model $\delta^{18}O$ and weighting by the monthly rainfall for each tributary (SI 7, Hengl, 2018). The uncertainty in $\delta^{18}O_{H_2O}$ was taken as inter-quartile range of these distributions (Fig. S4).

5. Partitioning Pyrite and Gypsum Derived Sulfate

After correction of $\delta^{34}S_{SO_4}$ and $\delta^{18}O_{SO_4}$ for atmospheric inputs, a binary mixing model was used to partition SO_4^{2-} inputs from the oxidation of sedimentary sulfides and sulfates using $\delta^{18}O_{SO_4}{}^*$ and $\delta^{18}O_{H_2O}$. The model was used firstly to calculate the fraction of riverine SO_4^{2-} derived from the oxidative weathering of pyrite and secondly the $\delta^{34}S$ of pyrite in the tributary catchments of the Mekong River. Finally, the main stem evolution of $\delta^{34}S_{SO_4}$ and $\delta^{18}O_{SO_4}$ were considered using a flux-weighted additive model to calculate f_{pyr} in the main river.

In the first order, the isotopic composition of the atmospheric corrected dissolved SO_4^{2-} is determined by the sum of the fractional contributions of SO_4^{2-} derived from gypsum (f_{gyp}) and pyrite (f_{pyr}) (Eqns. 9 and 10).

$$\delta^{18}O^*_{SO_4} = f_{gyp} \cdot \delta^{18}O_{SO_4 gyp} + f_{pyr} \cdot \delta^{18}O_{SO_4 pyr} \quad (9)$$

$$f_{pyr} = 1 - f_{gyp} \quad (10)$$

As discussed in Section 4.2, the oxygen and sulfur isotopic composition of the gypsum inputs are relatively well constrained, and the $\delta^{18}O_{SO_4}$ and $\delta^{34}S_{SO_4}$ of the average Cretaceous evaporite end-member in the Mekong basin were used in the model (Table 2). Since the global range in $\delta^{34}S_{SO_4\ pyr}$ spans > 100‰ (Fig. 1B, Strauss, 1997; Canfield, 2004) and, being a reactive phase it was not possible to extract any pyrite from suspended particulate matter for analysis, $\delta^{34}S_{SO_4}$ does not provide a similar constraint.

The oxygen isotope composition of the pyrite derived end-member ($\delta^{18}O_{SO_4\ pyr}$, Eqn. 7) was used to determine the fraction of sedimentary sulfate (f_{gyp}, and hence f_{pyr}) by combining the mass balance equations for oxygen in SO_4^{2-} (Eqns. 7, 9 and 10) to yield:

$$f_{gyp} = \frac{\delta^{18}O^*_{SO_4} - f_{O_2}\left(\delta^{18}O_{O_2} + \varepsilon_{SO_4-O_2}\right) - \left(1 - f_{O_2}\right)\left(\delta^{18}O_{H_2O} + \varepsilon_{SO_4-H_2O}\right)}{\delta^{18}O_{SO_4 gyp} - f_{O_2}\left(\delta^{18}O_{O_2} + \varepsilon_{SO_4-O_2}\right) - \left(1 - f_{O_2}\right)\left(\delta^{18}O_{H_2O} + \varepsilon_{SO_4-H_2O}\right)} \quad (11)$$

The calculated f_{gyp} and f_{pyr} were then substituted into the mass balance equation for $\delta^{34}S_{SO_4}{}^*$ to calculate a range of possible $\delta^{34}S$ values for pyrite that have contributed to the river chemistry in each sub-basin:

$$\delta^{34}S_{SO_4 pyr} = \frac{\delta^{34}S^*_{SO_4} - f_{gyp}\left(\delta^{34}S_{SO_4 gyp}\right)}{f_{pyr}} \quad (12)$$

Eqns. 11 and 12 were solved for each tributary and the northern most sample of the mainstem (MEK17-107) where the discharge is smaller than many of the tributaries from the lower reach (Fig. 5). Uncertainties were determined by repeating the calculation 10,000 times, with each parameter randomly sampled within the normal (for measured parameters) or uniform (for unknown parameters) distributions detailed in Table 2. The distributions of the input parameters were designed to maximize the uncertainties. For example the range in $\delta^{18}O_{O_2}$ values were permitted to range from 23‰ to 70‰ and the rain correction of riverine SO_4^{2-} allows for a wide range in isotopic values of the rain. Because of this uncertainty structure, a small number of iterations have f_{gyp}> 1 and these iterations were not included in the final mean values. Calculated values of $\delta^{34}S_{SO_4\ pyr}$ outside the typical natural range -100‰ to +10‰ were also not included in the final mean values.

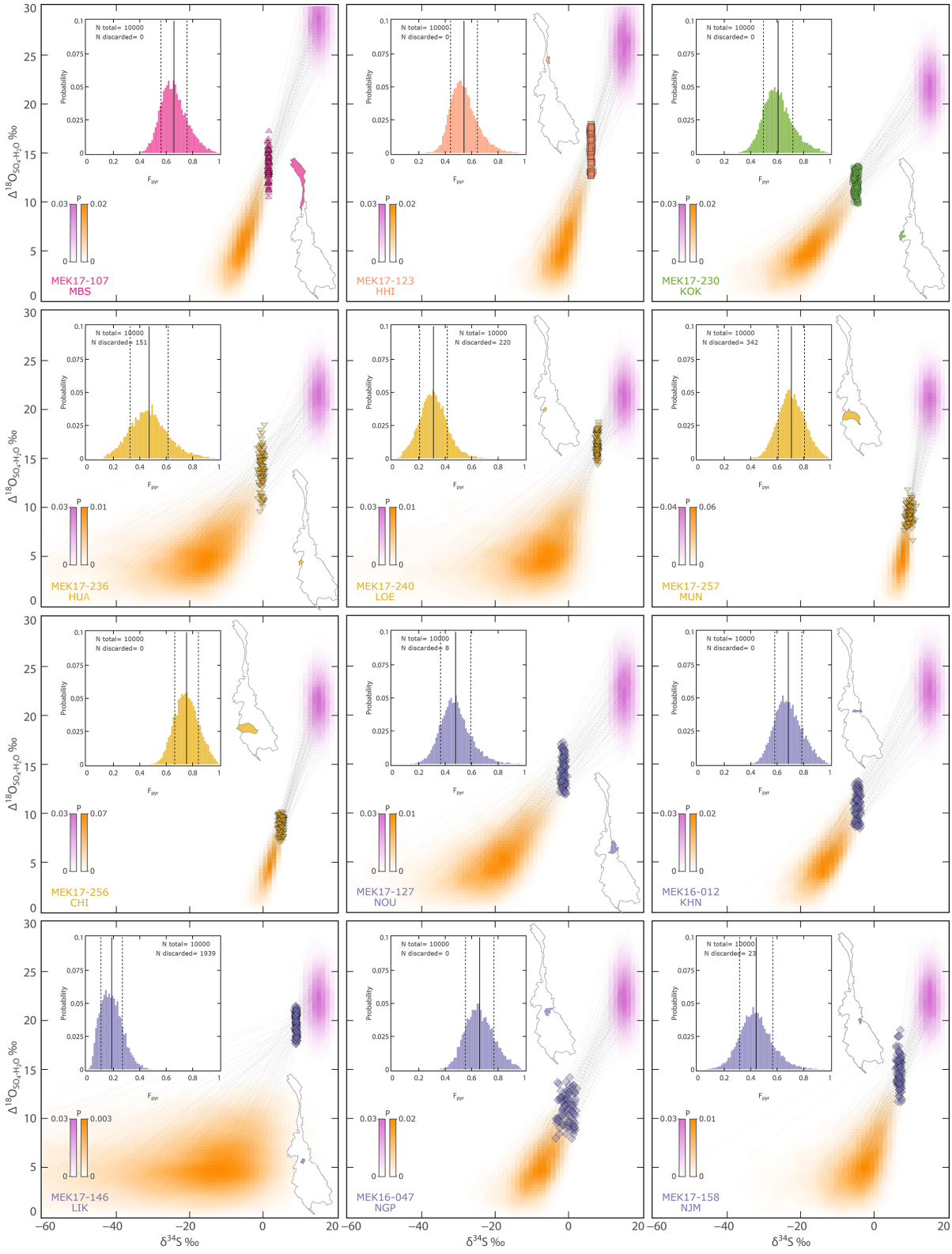

Figure 5 *(continues on next page)*: Summary of model outputs for all major tributaries plotted as $\delta^{34}S_{SO_4}{}^*$ vs the difference in $\delta^{18}O$ between sulfate and water ($\Delta^{18}O_{SO_4-H_2O}$). The complete distributions of gypsum and pyrite derived end-members are indicated by 2D probability density functions (pink and orange respectively). 100 water data points (randomly selected out of the 10000 total) are indicated to show the water sample and position of the mixing lines (dashed for that sample). Symbols and colors correspond to the legend in Fig 3. The range of f_{pyr} predicted by the uncertainty structure (Table 2) is shown by the inset histograms along with the mean and 1sd as dashed lines.

The number of iterations discarded was zero or insignificant (< 3.5%) except for one sample, where the uncertainty structure was amplified (discussed in more detail below). The model results of the mixing lines between gypsum and pyrite-derived SO_4^{2-} and the water samples (mixtures) are illustrated in Fig. 5, which also shows the distributions of calculated f_{pyr} values for each tributary.

5.1. Calculated $\delta^{34}S_{SO_4\ pyr}$ and uncertainties

The calculated $\delta^{34}S$ of SO_4^{2-} delivered by sulfide end-members ($\delta^{34}S_{SO_4\ pyr}$) ranges between -24‰ and +7‰ (Fig. 5, Table 1), well within the range of global sedimentary and igneous sulfide minerals (Fig. 1B). For most tributaries, $\delta^{34}S_{SO_4\ pyr}$ values have a 1sd uncertainty of less than 7‰, and the maximum 1sd uncertainty for any individual tributary is 21‰. Therefore, although the global range in $\delta^{34}S_{SO_4\ pyr}$ is large, the range of $\delta^{34}S_{SO_4\ pyr}$ that contribute SO_4^{2-} within a given tributary basin is relatively restricted. From Fig. 5 (e.g., sample MEK17-146, Nam Lik) it is qualitatively apparent that one of the dominant controls on the uncertainty of the calculated $\delta^{34}S_{SO_4\ pyr}$ is the relative values of $\delta^{34}S_{SO_4}{}^*$ and $\delta^{18}O_{SO_4}{}^*$ of the water sample, compared to those of the gypsum end-member. When there is a small difference between the water and gypsum (corresponding to a small f_{pyr}) this leads to an amplification in the uncertainty in $\delta^{34}S_{SO_4\ pyr}$. If, on the other hand, the water sample $\delta^{34}S_{SO_4}{}^*$ and $\delta^{18}O_{SO_4}{}^*$ values are close to the $\delta^{18}O_{SO_4}$ values of the pyrite derived end-member (e.g., sample MEK16-053, Nam Hinboun) the uncertainty on $\delta^{34}S_{SO_4\ pyr}$ is smaller (Fig. S8).

5.2. Fraction of sedimentary sulfide-derived sulfate in the Mekong river

There is a wide range in f_{pyr} in the Mekong River tributaries, from 0.19 to 0.84 (expressed as a fraction of *total* dissolved SO_4^{2-} where $f_{pyr} + f_{gyp} + f_{rain} = 1$, Fig. 6A, B & C, Table 1). The average and maximum 1σ uncertainties on f_{pyr} estimated from the Monte-Carlo simulation are 0.09 and 0.14 respectively, despite the large allowances for the input parameters. The uncertainty on f_{pyr} has a parabolic relationship with its absolute value (Fig. S8B) such that the uncertainty is at a maximum when $f_{pyr} = 0.5$.

In the upper Mekong, SO_4^{2-} concentrations are among the highest found in the basin. In the Heihui tributary (HHI) $f_{pyr} = 0.54 \pm 0.10$ (1σ) indicating SO_4^{2-} is sourced in almost equal quantities from oxidative weathering of pyrite and dissolution of evaporite minerals, with a very low contribution from rain (fractional contribution of < 0.02). The lithology is predominantly Jurassic marine units but with a large area of Pre-Cambrian metasedimentary rocks likely to contain pyrite. In the upper main river site at Baoshan (MBS) (where the discharge is lower than many of the tributaries in the lower reaches of the Mekong), $f_{pyr} = 0.66 \pm 0.10$ (1σ), reflecting pyrite-rich lithologies in the Mekong basin upstream of this sample. This is an important conclusion, firstly because the upper reaches contribute a significant SO_4^{2-} flux to the rest of the Mekong River, and secondly because the relatively high Cl^- concentrations are indicative of halite weathering but the high f_{pyr} values demonstrates that evaporites are only a secondary source of SO_4^{2-}.

In the middle section of the basin, tributaries draining the east bank of the Mekong in Laos show the largest range in f_{pyr} values, from 0.19 to 0.84. The tributaries with the highest f_{pyr} are the Nam Hinboun ($f_{pyr} = 0.81 \pm 0.08$ 1σ) and Nam Kading ($f_{pyr} = 0.84 \pm 0.08$ 1σ) which drain Triassic to Jurassic and Carboniferous to Permian limestone units where pyrite is common, as well as draining Palaeozoic igneous units of the Annamite mountain range (Ponta & Aharon, 2014). Although f_{pyr} is high, the SO_4^{2-} concentration of these tributaries is < 28 μmol/L.

The tributary with the highest proportion of SO_4^{2-} derived from the dissolution of sedimentary sulfate minerals ($f_{gyp} = 0.81 \pm 0.08$ 1σ) is the Nam Lik, with an order of magnitude greater SO_4^{2-} concentration than the surrounding tributaries indicating the presence of evaporite within the Permian marine units. This result shows the value of the mixing model presented here, since otherwise this high SO_4^{2-} concentration could have been mis-interpreted as being derived from the oxidative weathering of pyrite.

One of the largest tributaries in the region is the Nam Ou, where Cretaceous to Jurassic gypsum units and pyrite within Devonian to Permian limestones units have been reported. The f_{pyr} value 0.49 ± 0.12 (1σ) indicates an equal contribution to the SO_4^{2-} flux from both pyrite and gypsum weathering, but the low SO_4^{2-} concentration (27 μmol/L) demonstrates their contribution is minor.

On the west bank of the middle Mekong basin, the Mae Kok drains Devonian to Carboniferous shales and limestones with $f_{pyr} = 0.61 \pm 0.11$ (1σ). Tributaries in northern Thailand, Hueang and Loei, with contrasting SO_4^{2-} concentrations of 35 and 208 μmol/L, have low f_{pyr} values (0.47 and 0.31, respectively) due to high SO_4^{2-} contributions from Carboniferous anhydrite-gypsum deposits (Pisutha-Arnond *et al.*, 1986; Surakotra *et al.*, 2018).

A significant proportion of the bedrock on the west bank of the middle Mekong in Thailand comprises evaporite units (Chinese Academy of Geological Sciences, 1975). However, the calculated f_{pyr} values suggest that approximately one third of the SO_4^{2-} delivered by the Mun, Chi, and Songkhram rivers (f_{pyr} values of 0.71, 0.75 and 0.78 respectively) is sourced from these sulfate minerals. The vast majority of SO_4^{2-} on the Khorat Plateau appears to come from oxidative weathering of pyrite. Catchments containing sedimentary sulfate minerals generally have high SO_4^{2-} concentrations but this is not the case in the Mun, Chi and Songkhram (SO_4^{2-} < 25 μmol/L). In contrast Cl^- concentrations are between 412 to 816 μmol/L, indicating the dominant evaporite mineral being weathered is halite. The Maha Sarakham evaporite formation is underlain by the Mesozoic Khorat Group which comprises sandstone, siltstone and shale units. These terrigenous units contain abundant disseminated pyrite and some galena and sphalerite (Tabakh *et al.*, 1998) which likely contribute the high fraction of sulfide-derived SO_4^{2-} in the Mun, Chi, and Songkhram rivers. This counter-intuitive observation demonstrates that care needs to be taken in using published geological maps to infer CO_2

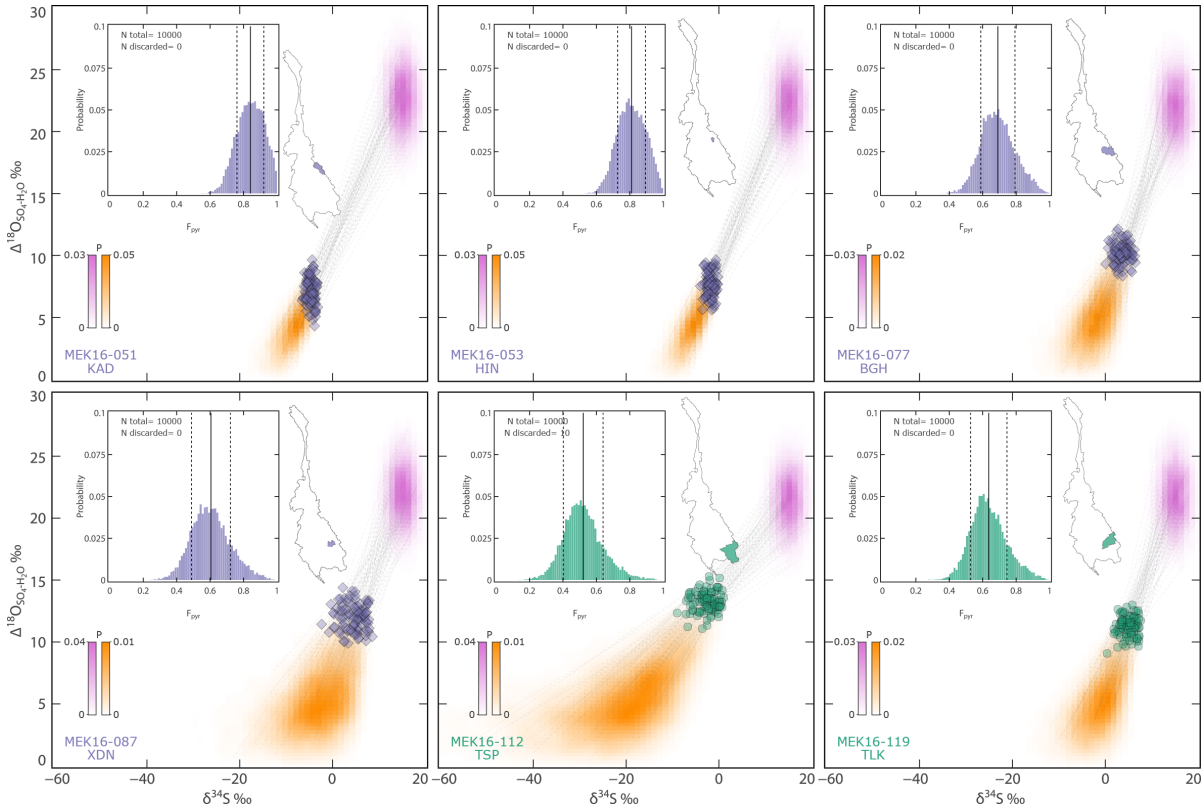

Figure 5 *(continued)*

consumption budgets based on global geology (Amiotte Suchet *et al.*, 2003).

The Tonle Srepok drains Triassic to Jurassic marine units and Pliocene to Quaternary basalts in northeastern Cambodia and has a f_{pyr} value of 0.53 ± 0.12 (1σ). The Tonle Kong has an f_{pyr} value of 0.64 ± 0.11 (1σ). These rivers, sampled at peak monsoon have the largest fraction of SO_4^{2-} derived from rain, at up to 30%.

5.3. Model limitations

The binary mixing model presented here does not take into account secondary processes such as bacterial sulfate reduction (BSR). BSR can significantly alter the isotopic composition of dissolved SO_4^{2-} due to the large isotope fractionations between sulfate and sulfide (Detmers *et al.*, 2001; Turchyn *et al.*, 2013) and references therein. BSR increases $\delta^{34}S_{SO_4}$ and $\delta^{18}O_{SO_4}$ values in river waters and could theoretically be occurring on the flood plains without sulfides being eroded and transported into the river in particulate form. Since BSR increases riverine $\delta^{34}S_{SO_4}$ and $\delta^{18}O_{SO_4}$ values it would cause the mixing model presented here to calculate a greater contribution from evaporite minerals; therefore our f_{pyr} values should be considered minimum estimates.

The rain correction used here does not account for evapo-transpiration. Although many of the samples have zero Cl^- after rain correction, it is still possible that the atmospheric inputs calculated here are an under-estimate. Whilst we have not considered additional anthropogenic inputs, in the peak monsoon conditions Cl^- concentrations do not increase downstream of cities, suggesting that in the present sample set anthropogenic inputs are minor.

The binary mixing approach developed above is appropriate over relatively restricted basin sizes, with limited latitudinal and elevation ranges over which the GNIP model for $\delta^{18}O$ in precipitation can be reliably used to constrain a unique $\delta^{18}O_{SO_4\,pyr}$. However, the mainstem $\delta^{18}O_{SO_4}$, $\delta^{18}O_{H_2O}$ and f_{pyr} values correspond to the integrated inputs from all upstream tributaries, which can contribute markedly different SO_4^{2-} fluxes to the mainstem, and therefore a different approach must be taken to calculate an f_{pyr} value for mainstem SO_4^{2-}.

5.4. Mixing evolution on the mainstem

The mainstem was divided into 6 regions (Fig. S9B) constrained by 6 monitoring stations on the main river where the Mekong River Commission has long-term records of both discharge and SO_4^{2-} concentrations (Mekong River Commission, 2016). For each region the total SO_4^{2-} flux from that region corresponds to the difference in SO_4^{2-} flux determined from the sampling station at the exit and entrance to that region. This total regional SO_4^{2-} flux is supplied by tributaries (some of which have f_{pyr} determined) as well as tributaries where either f_{pyr}, SO_4^{2-} or discharge were not measured, in addition to unknown inputs from groundwaters. The f_{pyr}, f_{gyp} and f_{rain} values for a region on the main river

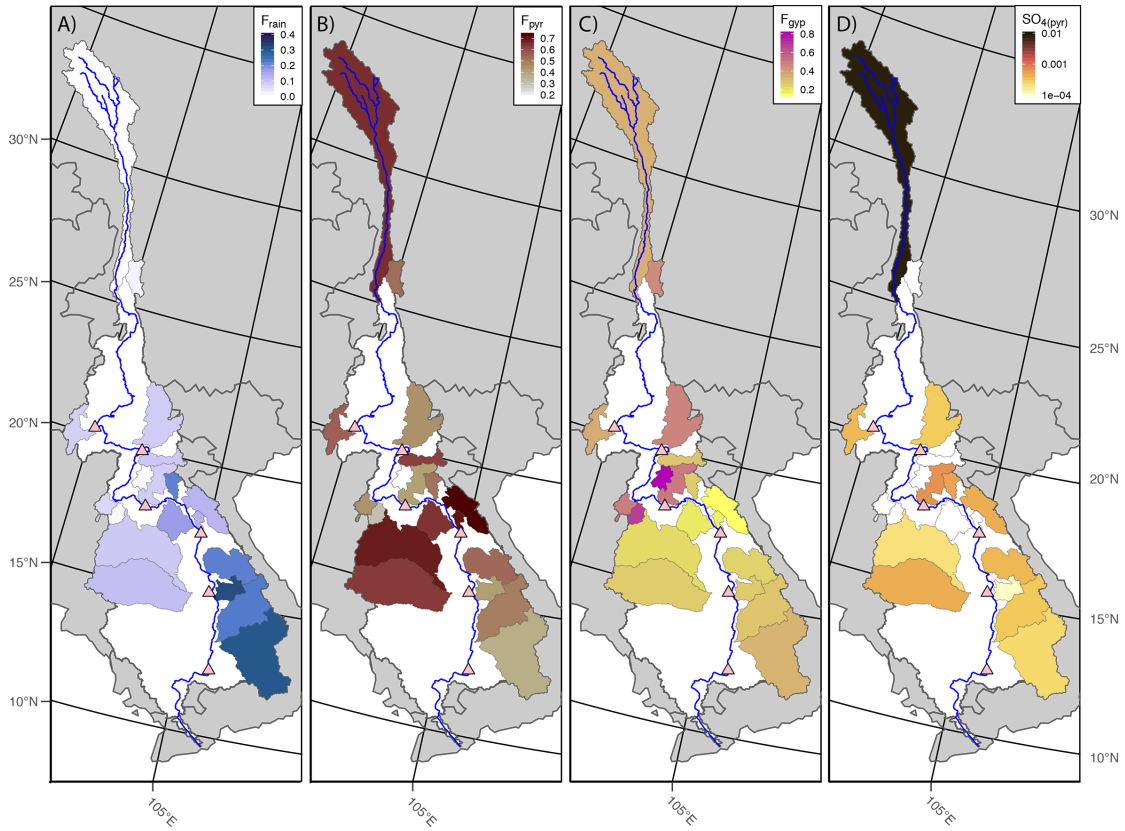

Figure 6: Variable source of SO_4^{2-} in the Mekong river basin. Tributary basins are coloured for A) f_{rain}, B), f_{pyr}, C) f_{gyp} and D the pyrite derived SO_4^{2-} flux in Mol/s/km^2. No discharge data available for missing tributary catchments (white) on panel D. Mainstem monitoring stations shown as pink triangles.

were determined by summing the flux weighted fractional inputs from tributaries between sites on the mainstem where SO_4^{2-} fluxes were known (SI 12). The f_{pyr} of the unknown flux was estimated by randomly sampling a uniform distribution between available f_{pyr} values of the tributaries from that region with the SO_4^{2-} flux given by the difference between the downstream and upstream mainstem sampling points and the total flux from the sampled tributaries. There is a covariance in the SO_4^{2-} fluxes between the up-stream and down-stream sampling stations on the main river because the fluxes exhibit large variations on daily to seasonal timescales which propagate down the river from source to sink (Fig. S10). This was accounted for in the uncertainty estimate by determining the covariance matrix on the SO_4^{2-} fluxes at each of 6 main river monitoring stations for the Mekong River Commission data set (1985-2000, filtered for charge balance, Mekong River Commission, 2016). The rain, pyrite and gypsum SO_4^{2-} fluxes were calculated between two mainstem sampling sites given the difference in SO_4^{2-} fluxes and the estimates of tributary compositions. The uncertainties were calculated from 10000 Monte Carlo iterations using a multivariate Gaussian distribution accounting for the covariance in the SO_4^{2-} fluxes at each of the mainstem sampling sites (SI 12).

In this way the cumulative flux and attendant uncertainty were determined at each of the 6 monitoring stations on the main river for the SO_4^{2-} flux derived from rain, gypsum and pyrite (Fig. S11). For the main river, $\delta^{34}S_{SO_4}$ and $\delta^{18}O_{SO_4}$ were calculated in the same way and compared to measured data for each station where the data exists. There is good agreement between the modelled and measured values (Fig. 3E and F). The flux weighted mean f_{pyr} for the entire basin was determined as 0.56 ± 0.07 (1σ).

5.5. *Controls on* f_{pyr}

Pyrite-derived SO_4^{2-} fluxes are high in the upper reaches of the Mekong (Fig. 6D), reflected in the high concentrations of riverine SO_4^{2-} (Fig. 3B). Although concentrations of SO_4^{2-} are low in tributaries in the middle and lower Mekong, the high discharge of these tributaries means there is a continual addition of pyrite-derived SO_4^{2-} flux downstream. In excess of 50% of the pyrite-derived SO_4^{2-} flux is delivered from the upper reaches of the Mekong with $< 8\%$ derived from the lower reaches between Khong Chiam and Kratie via the Khorat Plateau and the major Tonle Srepok and Tonle Kong tributaries (Fig. 6D).

Previous work has determined a strong link between the supply of material through erosion and the pyrite-derived SO_4^{2-} flux (Calmels *et al.*, 2007; Torres *et al.*, 2016). The pyrite derived fluxes determined in the present study are consistent with this idea, with the highest pyrite derived SO_4^{2-} fluxes in the high-elevation headwaters. It is worth noting however that the f_{pyr} values from the geologically complex Mekong river basin are ultimately controlled by rock type (Fig. S12), with

almost 50% of SO_4^{2-} in the mountainous headwaters controlled by gypsum and anhydrite weathering.

5.6. Implications for the carbon cycle

Li *et al.* (2014) used an archive database (Mekong River Commission, 2016) to estimate the long-term atmospheric CO_2 consumption in the Mekong via the weathering of Ca and Mg silicates determining a net carbon sink of almost 39 x 10^3 mol CO_2 km^{-1} yr^{-1} (Ca and Mg fluxes only, not including Na and K). Accounting for 56% of SO_4^{2-} being derived from the oxidative weathering of pyrite and assuming that sulfuric acid weathers carbonate minerals (Eqn. 1) much faster than silicate minerals would reduce this estimate to < 12 x 10^3 mol CO_2 km^{-1} yr^{-1}, a reduction of ~70% (SI S14). Repeating this calculation with the mean of the data from Kratie (the most downstream mainstem site) from the present study yields a very similar overall CO_2 consumption at ~ 14 x 10^3 mol CO_2 km^{-1} yr^{-1}. These estimates of CO_2 consumption by silicate weathering (and their uncertainty) require verification with flux weighted models accounting for the tributary silicate weathering fluxes using a similar approach to SO_4^{2-} fluxes in the main river used in the present study, but the estimated net reduction in CO_2 consumption via silicate weathering, even in a mixed lithology large river basin with low SO_4^{2-} concentrations is large. This raises questions over the magnitude of the silicate weathering climate feed-back (c.f. Tipper *et al.*, 2021) that will require similar studies in other large river basins

6. Conclusion

A new data set of $\delta^{34}S_{SO_4}$, $\delta^{18}O_{H_2O}$ and $\delta^{18}O_{SO_4}$ values in one of the world's largest rivers, the Mekong, was used to partition riverine SO_4^{2-} between rain, pyrite, and gypsum derived sources. The oxidative weathering of pyrite accounts for 56 ± 7% (1σ) of the SO_4^{2-} flux that is delivered to the South China Sea by the Mekong, with individual tributary values between 19 and 84%.

If the sulfuric acid derived from pyrite oxidation primarily weathers carbonates, releasing CO_2 to the atmosphere, the CO_2 consumed by silicate weathering will be offset by 70%. Given that the Mekong is not a sulfate rich river, and is not dominated by the oxidative weathering of pyrite, the implication is that the carbon fluxes associated with silicate weathering of other large rivers are currently overestimated. Accounting for sulfuric acid weathering in chemical weathering calculations could significantly alter our understanding of CO_2 fluxes, particularly in catchments where carbonate weathering is high. Of the world's major rivers, a detailed carbon budget considering the sulfuric acid weathering of carbonates has so far only been demonstrated for the Mackenzie River (Horan *et al.*, 2019). Further detailed sample collection and SO_4^{2-} partitioning in global rivers is needed to calculate a more accurate chemical weathering carbon budget.

Acknowledgements

This research was funded by a Natural Environment Research Council (NERC), UK, PhD Studentship to K.E. Relph and by NERC Standard Grants (PI Tipper NE/P011659/1, NE/M001865/1). We thank B. Savoeun, Nakarath Travel, J. Chen and Y. Liu for fieldwork logistics assistance, R. Robinson, T. Perkins, R. Santos and L. Feng for assistance in the collection of samples and discussions, J. Rolfe and H.J. Bradbury for analytical assistance and R.G. Hilton and C. Hackney for discussions. Chris Parish constructed all the field sampling equipment that made this possible. Lou Derry, Xin Gu and one anonymous reviewers are thanked for their thoughtful and astute comments which greatly improved this work.

References

Amiotte Suchet, P., Probst, J., & Ludwig, W., 2003. Worldwide distribution of continental rock lithology: Implications for the atmospheric/soil CO_2 uptake by continental weathering and alkalinity river transport to the oceans, *Global Biogeochemical Cycles*, **17**(2).

Angert, A., Luz, B., & Yakir, D., 2001. Fractionation of oxygen isotopes by respiration and diffusion in soils and its implications for the isotopic composition of atmospheric O_2, *Global Biogeochemical Cycles*, **15**(4), 871–880.

Balci, N., Shanks, W. C., Mayer, B., & Mandernack, K. W., 2007. Oxygen and sulfur isotope systematics of sulfate produced by bacterial and abiotic oxidation of pyrite, *Geochimica et Cosmochimica Acta*, **71**(15), 3796 – 3811.

Bao, H., 2006. Purifying barite for oxygen isotope measurement by dissolution and reprecipitation in a chelating solution, *Analytical Chemistry*, **78**(1), 304–309.

Bickle, M. J., Chapman, H. J., Tipper, E., Galy, A., De La Rocha, C. L., & Ahmad, T., 2018. Chemical weathering outputs from the flood plain of the Ganga, *Geochimica et Cosmochimica Acta*, **225**, 146–175.

Borges, J. B., Huh, Y., Moon, S., & Noh, H., 2008. Provenance and weathering control on river bed sediments of the eastern Tibetan Plateau and the Russian Far East, *Chemical Geology*, **254**(1–2), 52 – 72.

Brantley, S. L., Holleran, M. E., Jin, L., & Bazilevskaya, E., 2013. Probing deep weathering in the Shale Hills Critical Zone Observatory, Pennsylvania (USA): the hypothesis of nested chemical reaction fronts in the subsurface, *Earth Surface Processes and Landforms*, **38**(11), 1280–1298.

Burke, A., Present, T. M., Paris, G., Rae, E. C., Sandilands, B. H., Gaillardet, J., Peucker-Ehrenbrink, B., Fischer, W. W., McClelland, J. W., Spencer, R. G., Voss, B. M., & Adkins, J. F., 2018. Sulfur isotopes in rivers: Insights into global weathering budgets, pyrite oxidation, and the modern sulfur cycle, *Earth and Planetary Science Letters*, **496**, 168 – 177.

Calmels, D., Gaillardet, J., Brenot, A., & France-Lanord, C., 2007. Sustained sulfide oxidation by physical erosion processes in the Mackenzie River basin: Climatic perspectives, *Geology*, **35**(11), 1003–1006.

Canfield, D. E., 2004. The evolution of the Earth surface sulfur reservoir, *American Journal of Science*, **304**(10), 839–861.

Chinese Academy of Geological Sciences, C., 1975. *Geological Map of Asia, Scale: 1:5,000,000.*, Cartographic Publishing House, Beijing.

Claypool, G. E., Holser, W. T., Kaplan, I. R., Sakai, H., & Zak, I., 1980. The age curves of sulfur and oxygen isotopes in marine sulfate and their mutual interpretation, *Chemical Geology*, **28**, 199 – 260.

Crockford, P. W., Kunzmann, M., Bekker, A., Hayles, J., Bao, H., Halverson, G. P., Peng, Y., Bui, T. H., Cox, G. M., Gibson, T. M., Wörndle, S., Rainbird, R., Lepland, A., Swanson-Hysell, N. L., Master, S., Sreenivas, B., Kuznetsov, A., Krupenik, V., & Wing, B. A., 2019. Claypool continued: Extending the isotopic record of sedimentary sulfate, *Chemical Geology*, **513**, 200 – 225.

Dai, A. & Trenberth, K. E., 2002. Estimates of freshwater discharge from continents: Latitudinal and seasonal variations, *Journal of Hydrometeorology*, **3**(6), 660–687.

Detmers, J., Brüchert, V., Habicht, K. S., & Kuever, J., 2001. Diversity of sulfur isotope fractionations by sulfate-reducing prokaryotes, *Applied and Environmental Microbiology*, **67**(2), 888–894.

Francois, L. M. & Walker, J. C., 1992. Modelling the Phanerozoic carbon cycle and climate: constraints from the $^{87}Sr/^{86}Sr$ isotopic ratio of seawater, *American Journal of Science*, **292**(2), 81–135.

Galy, A. & France-Lanord, C., 1999. Weathering processes in the Ganges–Brahmaputra basin and the riverine alkalinity budget, *Chemical Geology*, **159**(1), 31–60.

Garzanti, E. & Resentini, A., 2016. Provenance control on chemical indices of weathering (Taiwan river sands), *Sedimentary Geology*, **336**, 81 – 95.

Gu, X., Heaney, P. J., Reis, F. D. A. A., & Brantley, S. L., 2020. Deep abiotic weathering of pyrite, *Science*, **370**(6515), eabb8092.

Gupta, A. & Liew, S., 2007. The Mekong from satellite imagery: A quick look at a large river, *Geomorphology*, **85**(3–4), 259 – 274.

Han, X., Guo, Q., Liu, C., Fu, P., Strauss, H., Yang, J., Hu, J., Wei, L., Ren, H., Peters, M., Wei, R., & Tian, L., 2016. Using stable isotopes to trace sources and formation processes of sulfate aerosols from Beijing, China, *Scientific Reports*, **6**(1), 29958.

Heidel, C. & Tichomirowa, M., 2011. The isotopic composition of sulfate from anaerobic and low oxygen pyrite oxidation experiments with ferric iron – New insights into oxidation mechanisms, *Chemical Geology*, **281**(3), 305 – 316.

Hemingway, J. D., Olson, H., Turchyn, A. V., Tipper, E. T., Bickle, M. J., & Johnston, D. T., 2020. Triple oxygen isotope insight into terrestrial pyrite oxidation, *Proceedings of the National Academy of Sciences*, **117**(14), 7650–7657.

Hengl, T., 2018. Monthly precipitation in mm at 1 km resolution based on SM2RAIN-ASCAT 2007-2018, IMERGE, CHELSA Climate and WorldClim.

Hindshaw, R. S., Heaton, T. H., Boyd, E. S., Lindsay, M. R., & Tipper, E. T., 2016. Influence of glaciation on mechanisms of mineral weathering in two high Arctic catchments, *Chemical Geology*, **420**, 37 – 50.

Horan, K., Hilton, R. G., Dellinger, M., Tipper, E., Galy, V., Calmels, D., Selby, D., Gaillardet, J., Ottley, C. J., Parsons, D. R., & Burton, K. W., 2019. Carbon dioxide emissions by rock organic carbon oxidation and the net geochemical carbon budget of the Mackenzie River Basin, *American Journal of Science*, **319**(6), 473–499.

Jiang, H., Li, W.-Q., Jiang, S.-Y., Wang, H., & Wei, X.-P., 2017. Geochronological, geochemical and Sr-Nd-Hf isotopic constraints on the petrogenesis of Late Cretaceous A-type granites from the Sibumasu Block, Southern Myanmar, SE Asia, *Lithos*, **268-271**, 32 – 47.

Kemeny, P. C., Lopez, G. I., Dalleska, N. F., Torres, M., Burke, A., Bhatt, M. P., West, A. J., Hartmann, J., & Adkins, J. F., 2021. Sulfate sulfur isotopes and major ion chemistry reveal that pyrite oxidation counteracts CO_2 drawdown from silicate weathering in the Langtang-Trisuli-Narayani River system, Nepal Himalaya$_2$ drawdown from silicate weathering in the Langtang-Trisuli-Narayani River system, Nepal Himalaya, *Geochimica et Cosmochimica Acta*, **294**, 43–69.

Kiernan, K., 2015. Karst geomorphology along the Nam Ou, northern Lao PDR, *Cave and Karst Science*, **42**(2), 86–94.

Kim, H., Stinchcomb, G., & Brantley, S. L., 2017. Feedbacks among O_2 and CO_2 in deep soil gas, oxidation of ferrous minerals, and fractures: A hypothesis for steady-state regolith thickness, *Earth and Planetary Science Letters*, **460**, 29–40.

Kroopnick, P. & Craig, H., 1972. Atmospheric Oxygen: Isotopic Composition and Solubility Fractionation, *Science*, **175**(4017), 54–55.

Lang, K. A., Huntington, K. W., Burmester, R., & Housen, B., 2016. Rapid exhumation of the eastern Himalayan syntaxis since the late Miocene, *Bulletin*, **128**(9-10), 1403–1422.

Li, C. & Ji, H., 2016. Chemical weathering and the role of sulfuric and nitric acids in carbonate weathering: Isotopes (^{13}C, ^{15}N, ^{34}S, and ^{18}O) and chemical constraints, *Journal of Geophysical Research: Biogeosciences*, **121**(5), 1288–1305.

Li, S., Lu, X., & Bush, R. T., 2014. Chemical weathering and CO_2 consumption in the Lower Mekong River, *Science of The Total Environment*, **472**, 162 – 177.

Li, S.-L., Calmels, D., Han, G., Gaillardet, J., & Liu, C.-Q., 2008. Sulfuric acid as an agent of carbonate weathering constrained by $\delta^{13}C_{DIC}$: Examples from Southwest China, *Earth and Planetary Science Letters*, **270**(3–4), 189 – 199.

Mekong River Commission, M., 2016. MRC Master Catalogue Search, (http://portal.mrcmekong.org/search/search).

Menz, F. C. & Seip, H. M., 2004. Acid rain in Europe and the United States: an update, *Environmental Science & Policy*, **7**(4), 253 – 265.

Noh, H., Huh, Y., Qin, J., & Ellis, A., 2009. Chemical weathering in the Three Rivers region of Eastern Tibet, *Geochimica et Cosmochimica Acta*, **73**(7), 1857 – 1877.

Pisutha-Arnond, V., Chiba, H., & Yumuang, S., 1986. A preliminary sulphur and oxygen isotope study of the Maha Sarakham evaporitic anhydrite from the Bamnet Narong area of northeastern Thailand, *Geological Society of Malaysia*, **1**(19), 209–222.

Ponta, G. M. & Aharon, P., 2014. Karst geology and isotope hydrology of the upstream section of Nam Hinboun River, Khammouan Province (Central Laos), *Carbonates and Evaporites*, **29**(1), 127–139.

Rennie, V. C. F. & Turchyn, A. V., 2014. Controls on the abiotic exchange between aqueous sulfate and water under laboratory conditions, *Limnology and Oceanography: Methods*, **12**(4), 166–173.

Robinson, B. W. & Bottrell, S. H., 1997. Discrimination of sulfur sources in pristine and polluted New Zealand river catchments using stable isotopes, *Applied Geochemistry*, **12**(3), 305 – 319.

Spence, J. & Telmer, K., 2005. The role of sulfur in chemical weathering and atmospheric CO_2 fluxes: Evidence from major ions, $\delta^{13}C_{DIC}$, and $\delta^{34}S_{SO4}$ in rivers of the Canadian Cordillera, *Geochimica et Cosmochimica Acta*, **69**(23), 5441 – 5458.

Strauss, H., 1997. The isotopic composition of sedimentary sulfur through time, *Palaeogeography, Palaeoclimatology, Palaeoecology*, **132**(1), 97 – 118.

Surakotra, N., Promkotra, S., Charusiri, P., Maruoka, T., & Hisada, K.-i., 2018. Sulfur, strontium, carbon, and oxygen isotopes of calcium sulfate deposits in late Carboniferous rocks of the Loei-Wang Saphung (LWS) Area, Loei Province, Thailand, *Geosciences*, **8**(7), 229.

Tabakh, M. E., Schreiber, B. C., Utha-Aroon, C., Coshell, L., & Warren, J. K., 1998. Diagenetic origin of basal anhydrite in the Cretaceous Maha Sarakham salt: Khorat Plateau, NE Thailand, *Sedimentology*, **45**(3), 579–594.

Tabakh, M. E., Utha-Aroon, C., & Schreiber, B., 1999. Sedimentology of the Cretaceous Maha Sarakham evaporites in the Khorat Plateau of northeastern Thailand, *Sedimentary Geology*, **123**(1), 31 – 62.

Taylor, B. E., Wheeler, M. C., & Nordstrom, D. K., 1984. Isotope composition of sulphate in acid mine drainage as measure of bacterial oxidation, *Nature*, **308**(5959), 538–541.

Taylor, B. E., Wheeler, M. C., & Nordstrom, D. K., 1984. Stable isotope geochemistry of acid mine drainage: Experimental oxidation of pyrite, *Geochimica et Cosmochimica Acta*, **48**(12), 2669 – 2678.

Terzer, S., Wassenaar, L. I., Araguás-Araguás, L. J., & Aggarwal, P. K., 2013. Global isoscapes for $\delta^{18}O$ and $\delta^{2}H$ in precipitation: improved prediction using regionalized climatic regression models, *Hydrol. Earth Syst. Sci.*, **17**(11), 4713–4728.

Thode, H., 1991. *Stable Isotopes in the Assessment of Natural and Anthropogenic Sulphur in the Environment*, chap. Sulphur isotopes in nature and the environment: an overview, pp. 1–26, John Wiley & Sons, Ltd.

Tipper, E. T., Bickle, M. J., Galy, A., West, A. J., Pomiès, C., & Chapman, H. J., 2006. The short term climatic sensitivity of carbonate and silicate weathering fluxes: Insight from seasonal variations in river chemistry, *Geochimica et Cosmochimica Acta*, **70**(11), 2737 – 2754.

Tipper, E. T., Stevenson, E. I., Alcock, V., Knight, A. C. G., Baronas, J. J., Hilton, R. G., Bickle, M. J., Larkin, C. S., Feng, L., Relph, K. E., & Hughes, G., 2021. Global silicate weathering flux overestimated because of sediment–water cation exchange, *Proceedings of the National Academy of Sciences*, **118**(1), e2016430118.

Torres, M. A., West, A. J., & Li, G., 2014. Sulphide oxidation and carbonate dissolution as a source of CO_2 over geological timescales, *Nature*, **507**(7492), 346–349.

Torres, M. A., West, A. J., Clark, K. E., Paris, G., Bouchez, J., Ponton, C., Feakins, S. J., Galy, V., & Adkins, J. F., 2016. The acid and alkalinity budgets of weathering in the Andes–Amazon system: Insights into the erosional control of global biogeochemical cycles, *Earth and Planetary Science Letters*, **450**, 381 – 391.

Turchyn, A. V., Tipper, E. T., Galy, A., Lo, J.-K., & Bickle, M. J., 2013. Isotope evidence for secondary sulfide precipitation along the Marsyandi River, Nepal, Himalayas, *Earth and Planetary Science Letters*, **374**, 36 – 46.

van Everdingen, R. O. & Krouse, H. R., 1985. Isotope composition of sulphates generated by bacterial and abiological oxidation, *Nature*, **315**(6018), 395–396.

Walker, J. C. G., Hays, P. B., & Kasting, J. F., 1981. A negative feedback mechanism for the long-term stabilization of Earth's surface temperature, *Journal of Geophysical Research: Oceans*, **86**(C10), 9776–9782.

Wu, W., Xu, S., Yang, J., & Yin, H., 2008. Silicate weathering and CO_2 consumption deduced from the seven Chinese rivers originating in the Qinghai-Tibet Plateau, *Chemical Geology*, **249**(3–4), 307 – 320.